

Zebrafish oxytocin neurons drive nocifensive behavior via brainstem premotor targets

Caroline L. Wee^{1,2}, Maxim Nikitchenko¹, Wei-Chun Wang³, Sasha J. Luks-Morgan³, Erin Song¹, James A. Gagnon^{1,8}, Owen Randlett¹, Isaac H. Bianco^{1,9}, Alix M. B. Lacoste¹, Elena Glushenkova¹, Joshua P. Barrios³, Alexander F. Schier^{1,4,5,6,7}, Samuel Kunes¹, Florian Engert^{1*} and Adam D. Douglass^{1,3*}

Animals have evolved specialized neural circuits to defend themselves from pain- and injury-causing stimuli. Using a combination of optical, behavioral and genetic approaches in the larval zebrafish, we describe a novel role for hypothalamic oxytocin (OXT) neurons in the processing of noxious stimuli. In vivo imaging revealed that a large and distributed fraction of zebrafish OXT neurons respond strongly to noxious inputs, including the activation of damage-sensing TRPA1 receptors. OXT population activity reflects the sensorimotor transformation of the noxious stimulus, with some neurons encoding sensory information and others correlating more strongly with large-angle swims. Notably, OXT neuron activation is sufficient to generate this defensive behavior via the recruitment of brainstem premotor targets, whereas ablation of OXT neurons or loss of the peptide attenuates behavioral responses to TRPA1 activation. These data highlight a crucial role for OXT neurons in the generation of appropriate defensive responses to noxious input.

Specialized neural circuits that identify perceived threats, such as predators or pain, and drive evasive behaviors are found across all species and may form the basis for complex emotions in humans^{1,2}. While many elements of these circuits are context- and species-specific, nociceptive circuits share conserved sensory receptors, which could be used as entry points into elucidating pain-processing mechanisms³. However, downstream of peripheral sensory neurons, the central circuits involved in nociception and their interactions with motor networks that drive appropriate responses are still largely uncharacterized^{2,3}.

Increasing attention has been directed toward the hypothalamic neuropeptide OXT in the processing of noxious stimuli. While much better known for its sociosexual and affiliative roles, studies have shown that OXT has antinociceptive, anti-inflammatory and anxiolytic properties, and thus could ameliorate the perception of, or behavioral response to, painful or aversive experience^{4–6}. For example, a population of around 30 OXT neurons, out of thousands in the rodent hypothalamus, suppress the activity of spinal nociceptors both directly through spinal projections and indirectly by modulating the neuroendocrine release of OXT from other OXT subpopulations^{4,7}. A distinct amygdala-projecting subpopulation has also been shown to reduce pain-conditioned fear behaviors⁵. However, recent human studies have demonstrated that OXT in fact increases defensive responses to unpredictable electric shocks⁸ and acoustic startle stimuli⁹, indicating that it might be enhancing, rather than suppressing, defensive behaviors under some circumstances.

To understand these apparently contradictory functional roles, it is essential to determine how noxious stimuli are represented within the OXT population, and to relate these activity patterns to

behavioral output. The large size and experimental inaccessibility of mammalian OXT nuclei has made it difficult to address these issues, and few functional recordings of OXT neuronal activity have been made in behaving animals. Fortunately, OXT circuits are remarkably well conserved¹⁰. In fish, neurons producing isotocin, the ortholog of OXT (commonly referred to in the fish literature as OXT^{11–13}) are mainly located in the neurosecretory preoptic hypothalamic area, which is homologous to the paraventricular nucleus, the supraoptic nucleus and accessory nuclei of the hypothalamus in mammals^{10,14}. As in mammals, zebrafish OXT neurons project to the pituitary, where OXT is released as a neurohormone, and send axons to a broad range of neuronal targets throughout the forebrain, hindbrain and spinal cord^{11–13,15–17}.

Here, we use the larval zebrafish, in which the entire OXT population is both optically and genetically accessible, to dissect the role of OXT neurons in the processing of nociceptive inputs. We show that zebrafish OXT neurons respond in a graded fashion to a range of aversive stimuli, with noxious experience causing the strongest and broadest activation. Transient receptor potential cation channel, subfamily A, member 1 (TRPA1) receptor activation drives both OXT neuron firing and defensive swimming behavior in the form of large-angle tail bends, and both the sensory and motor components of this process are encoded in OXT population activity. Experimental activation of OXT cells or TRPA1 receptors recruits a common network of brainstem spinal-projecting neurons, including but not limited to the escape-promoting Mauthner cell (M-cell)¹⁸, to generate these behavioral responses. In contrast, loss of OXT function or ablation of OXT neurons attenuates TRPA1-evoked behavior. Thus, hypothalamic

¹Department of Molecular and Cellular Biology and Center for Brain Science, Harvard University, Cambridge, MA, USA. ²Program in Neuroscience, Department of Neurobiology, Harvard Medical School, Boston, MA, USA. ³Department of Neurobiology and Anatomy, University of Utah, Salt Lake City, UT, USA. ⁴Center for Brain Science, Harvard University, Cambridge, MA, USA. ⁵Broad Institute of MIT and Harvard, Cambridge, MA, USA. ⁶Harvard Stem Cell Institute, Cambridge, MA, USA. ⁷FAS Center for Systems Biology, Harvard University, Cambridge, MA, USA. ⁸Present address: Department of Biology, University of Utah, Salt Lake City, UT, USA. ⁹Present address: Department of Neuroscience, Physiology and Pharmacology, University College London, London, UK. *e-mail: florian@mcb.harvard.edu; adam.douglass@neuro.utah.edu

OXT neurons form an essential part of a sensorimotor circuit for nociception in zebrafish, and might play a broader role in the processing of aversive stimuli.

Results

Brain-wide activity mapping of nociceptive pathways in zebrafish.

To identify brain regions that process noxious information, we first utilized a MAP-mapping approach that relies on whole-brain imaging of phosphorylated ERK (pERK) as a marker of neuronal activity¹⁹. We found that the preoptic area (PO) and its neurosecretory target, the pituitary gland, were among a number of areas that were reliably and selectively activated by mustard oil, electric shock and noxious (37 °C) heat (Fig. 1a,b). A non-nociceptive but aversive vibrational–acoustic stimulus (dish taps)¹⁸ activated the PO less reliably (Fig. 1a,b). Other loci were activated by both noxious stimuli and dish taps, such as the caudal hypothalamus and the norepinephrine locus coeruleus, which suggests that they might play a more general role in aversion (Fig. 1a,b). The norepinephrine area postrema was activated by both mustard oil and food, which is consistent with its known roles in chemical sensation and food intake regulation²⁰.

OXT neurons respond in a graded manner to noxious and aversive stimuli. Since OXT neurons are the most numerous cell type in the zebrafish PO¹⁴, we determined whether they might play a role in nociception. We performed pERK staining on transgenic fish¹³ in which green fluorescent protein (GFP) is expressed specifically in OXT neurons in the PO (OXT_{PO}) and the neighboring posterior tuberculum (PT; OXT_{PT}) (Fig. 1c,d; Supplementary Fig 1). Indeed, pERK intensity was elevated in OXT neurons following stimulation with high-intensity electric shock, mustard oil and noxious heat (37 °C), with noxious heat showing the weakest activation (Fig. 2a–c). In contrast, mean pERK activity per fish in OXT neurons was not significantly changed by vibrational–acoustic tap stimuli. We also

observed widespread activation of some non-OXT neurons by noxious stimuli, especially in the anterior PO (aPO) (Figs. 1d and 2a–c). These activated neurons may produce corticotropin-releasing factor or arginine–vasotocin, or could be non-neuromodulatory cell types¹⁴. However, on average, a higher proportion of OXT neurons were activated by noxious stimuli than their neighbors (Fig. 2a,b).

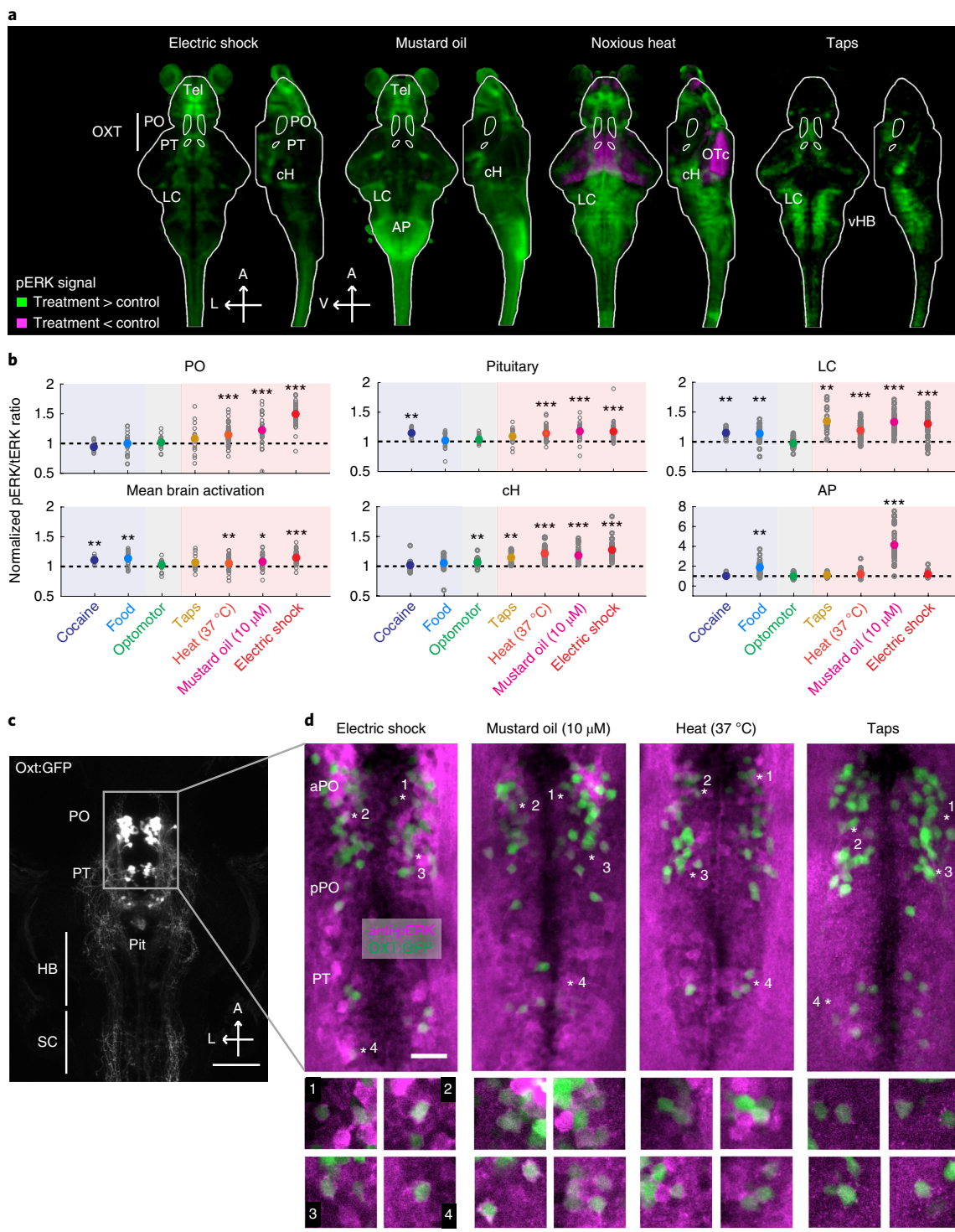
We confirmed these results by generating a driver line, *Tg(oxt:Gal4)*, and crossing it against a *Tg(UAS:GCaMP6s)* reporter to enable calcium imaging in OXT-expressing cells (Supplementary Figs. 2h and 3a,b). The same fish were exposed to shock, mustard oil, heat and taps to compare OXT responses across different sensory modalities. OXT neurons were responsive to all of the stimuli tested, although taps elicited responses of the weakest magnitude (Fig. 2d; Supplementary Fig. 3). Consistent with our pERK results, shock and mustard oil induced strong and widespread OXT neuron activation, while noxious heat induced intermediate levels of activation, which appeared to be stronger than predicted by pERK. Thus, OXT neurons respond in a graded fashion to a range of aversive inputs, with noxious stimuli causing the strongest and most widespread activation. Notably, there was a high degree of overlap between OXT cells responding to shock, mustard oil and heat, which suggests that multiple noxious inputs can be processed by the same neurons (Fig. 2d; Supplementary Fig. 3).

Magnocellular and parvocellular OXT neurons are activated by noxious stimuli. As in mammals, zebrafish OXT neurons comprise a diverse population that can be broadly divided into magnocellular and parvocellular classes^{11,12,21,22}. Magnocellular cells are larger, express higher levels of the OXT peptide and project to the pituitary, where OXT is released as a neurohormone. Parvocellular neurons are smaller, express less OXT and project to other regions of the CNS. In agreement with prior work^{11,12}, we found that magnocellular cells are located more anteriorly than parvocellular cells and are enriched within the PO (Supplementary Fig. 2).

Fig. 1 | Brain-wide responses to noxious and aversive stimuli. **a**, Whole-brain MAP-mapping experiments showing neural responses to a range of aversive stimuli. Each map was generated by pooling and analyzing data across multiple experiments to generate a composite map. Maps display voxels that are significantly activated (green) or inhibited (magenta) across multiple experiments: electric shock (three experiments), mustard oil (two 10 μM experiments and one 25 μM experiment), 37 °C heat (three experiments) and dish taps (two experiments). The brain is outlined in white, as are the PO and PT regions. Mustard oil treatment also induced pERK expression outside the brain, especially in skin and muscle tissue. These data include results from a previously published single experiment¹⁹, combined with these new experiments. Scale bar, 100 μm. In the maps: AP, area postrema; cH, caudal hypothalamus; LC, locus coeruleus; OTc, optic tectum; vHB, ventral hindbrain. For the arrows: A, anterior; L, left; V, ventral. **b**, Comparison of PO (upper leftmost) and whole brain (lower leftmost) activation in response to a range of appetitive (cocaine or food), neutral (optomotor gratings) and aversive (dish taps, 37 °C heat, mustard oil or electric shock) stimuli. Background shading represents stimulus valence (blue, positive; red, negative; gray, neutral). Broken black lines indicate a normalized treatment:control ratio of 1.0. Fold change in PO versus whole brain activity: 0.94 ± 0.03 versus 1.1 ± 0.01 (cocaine); 1.00 ± 0.04 versus 1.13 ± 0.02 (food); 1.02 ± 0.02 versus 1.02 ± 0.02 (optomotor); 1.08 ± 0.08 versus 1.06 ± 0.04 (taps); 1.14 ± 0.02 versus 1.04 ± 0.01 (heat); 1.22 ± 0.04 versus 1.08 ± 0.02 (mustard oil); 1.49 ± 0.03 versus 1.14 ± 0.02 (electric shock). Adjusted *P* values for these ratios are as follows: *P* = 0.19 versus ***P* = 0.003 (cocaine); *P* = 6.19 versus ***P* = 0.002 (food); *P* = 2.11 versus *P* = 0.36 (optomotor); *P* = 2.90 versus *P* = 1.51 (taps); ****P* = 4.77 × 10⁻⁶ versus ***P* = 0.008 (heat); ****P* = 2.13 × 10⁻⁴ versus **P* = 0.012 (10 μM mustard oil); ****P* = 4.30 × 10⁻⁷ versus ****P* = 1.70 × 10⁻⁶ (electric shock). *n* = 12 (cocaine), 22 (food), 23 (optomotor), 13 (taps), 50 (heat), 32 (mustard oil) and 39 (electric shock) fish pooled across multiple experiments, two-sided Wilcoxon signed-rank test against median of 1, Bonferroni corrected. Also shown are examples of other brain regions that were affected by aversive or noxious stimuli. The pituitary (hypophysis) showed significant enhancement in pERK signals for electric shock (1.17-fold, ****P* = 5.03 × 10⁻⁷), 10 μM mustard oil (1.18-fold, ****P* = 6 × 10⁻⁵), heat (1.14-fold, ****P* = 1.86 × 10⁻⁸) and cocaine (1.16-fold, ***P* = 0.0034). The norepinephrine LC showed strong activation by taps (1.34-fold, ***P* = 0.0017), mustard oil (1.32-fold, ****P* = 5.57 × 10⁻⁶) and electric shock (1.30-fold, ****P* = 8.98 × 10⁻⁶), and slightly weaker activation by heat (1.18-fold, ****P* = 4.73 × 10⁻⁸), cocaine (1.14-fold, ***P* = 0.0034) and food (1.13-fold, ***P* = 0.0097). The cH was significantly activated by electric shock (1.27-fold, *P* = 3.68 × 10⁻⁷), mustard oil (1.18-fold, *P* = 5.57 × 10⁻⁶), heat (1.21-fold, *P* = 5.29 × 10⁻⁹), taps (1.14-fold, ***P* = 0.0017), and more weakly by optomotor stimuli (1.06-fold, ***P* = 0.0014). The AP was highly activated by mustard oil (4.12-fold, ****P* = 6.13 × 10⁻⁶; note the change in the *y* scale) and relatively weakly by electric shock (1.17-fold, ****P* = 3.22 × 10⁻⁴). It is also strongly activated by food stimuli (1.85-fold, ***P* = 0.0011). **c**, *z*-projection image of *Tg(oxt:GFP)* fish showing OXT neurons in the PO and PT and their projections to the pituitary gland (Pit), hindbrain (HB) and spinal cord (SC), among other regions. Scale bar, 100 μm. **d**, Upper: *z*-projection images of dissected brain showing the overlap of OXT:GFP-positive neurons with pERK staining after 15 min of electric shock (30 s ISI, 100 ms shock, 6 V cm⁻¹, representative image of 2 datasets), mustard oil treatment (10 μM, representative image of 3 datasets), noxious heat (37 °C, representative image of 3 datasets) and taps (30 s ISI, representative image of 2 datasets). Results from these datasets are further analyzed in Fig. 2. Scale bar, 20 μm. Both OXT and surrounding non-OXT neurons were activated by these stimuli. Lower inset: examples of the putative overlap between OXT expression and pERK staining corresponding to regions indicated by numbered asterisks. Black scale bar (box width), 20 μm; white scale bar, 20 μm. pPO, posterior PO; aPO, anterior PO.

In both pERK and calcium imaging experiments, there was strong activation of OXT neurons by electric shock and mustard oil across the entire PO and PT clusters. There was weaker, but similarly distributed, activation by heat (Fig. 2c,d; Supplementary Fig. 3a,b), whereas dish taps activated more posterior (likely parvocellular) regions within the PO. Thus, noxious stimuli are potent activators of the zebrafish PO and PT, and appear to recruit a higher percentage of both magnocellular and parvocellular OXT neurons compared with other non-OXT cells in their vicinity.

TRPA1 activation induces nocifensive behavior in zebrafish. TRP cation channels function as tissue-damage sensors in insects, zebrafish and mammals^{23,24}. One major class of TRP ion channels, TRPA1, is activated by mustard oil, other chemical irritants and endogenous products of inflammation, whereas heat acts through the related TRPV1 receptor, although they overlap significantly in their expression patterns and functions^{25–27}. Since OXT neurons responded most strongly to mustard oil stimulation, we focused on TRPA1-mediated signals in our subsequent characterization of the role of OXT in nociception.



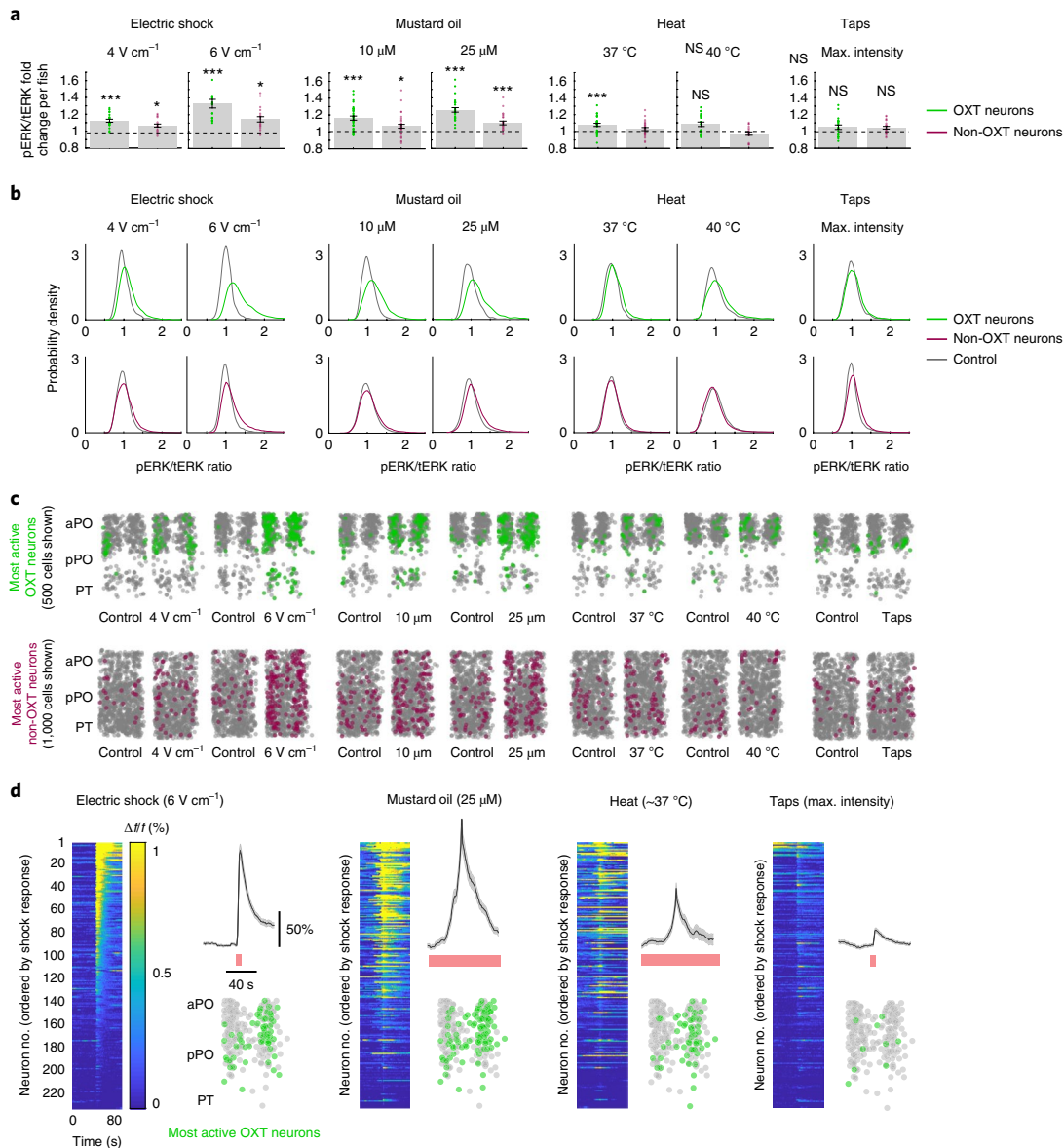


Fig. 2 | Cellular analysis of OXT activity reveals preferential activation by noxious stimuli. **a**, Fold change in mean OXT and neighboring non-OXT neuron pERK activity by fish, relative to controls. Data shown in this figure are from high-resolution images acquired from dissected brains. pERK/tERK ratios of individual *Tg(oxt:GFP)*-positive neurons were normalized to the mean pERK/tERK ratios of OXT neurons in control fish within each experiment and aggregated over multiple experiments. Shock 4 V cm⁻¹: ****P* = 6.16 × 10⁻⁵, fold increase = 1.12 (OXT), **P* = 0.02, fold increase = 1.06 (non-OXT), *n* = 14 control and 20 treatment; shock 6 V cm⁻¹: ****P* = 8.06 × 10⁻⁷, fold increase = 1.34 (OXT), ****P* = 2.63 × 10⁻⁴, fold increase = 1.15 (non-OXT), *n* = 19 control and 19 treatment; 10 μM mustard oil: ****P* = 1.42 × 10⁻⁶, fold increase = 1.17 (OXT), **P* = 0.0381, fold increase = 1.06 (non-OXT), *n* = 33 control and 35 treatment; 25 μM mustard oil: ****P* = 6.87 × 10⁻⁹, fold increase = 1.26 (OXT), ****P* = 3.08 × 10⁻⁴, fold increase = 1.11 (non-OXT), *n* = 25 control and 26 treatment; 37 °C heat: ****P* = 5.40 × 10⁻⁴, fold increase = 1.08 (OXT), *P* = 0.14, fold increase = 1.03 (non-OXT), *n* = 38 control and 32 treatment, 40 °C heat: *P* = 0.06, fold increase = 1.09 (OXT), *P* = 0.4, fold increase = 0.97 (non-OXT), *n* = 12 control and 19 treatment; taps: *P* = 0.12, mean increase = 1.05 (OXT), *P* = 0.09, mean increase = 1.05 (non-OXT), *n* = 22 control and 22 treatment, two-sided Wilcoxon rank-sum test. **b**, Probability distributions (kernel density estimate (KDE)) of pERK/tERK ratios for individual OXT (upper) and non-OXT (lower) neurons after treatment with noxious or aversive stimuli compared to control distributions (gray). Electric shock and mustard oil induced the strongest rightward shifts in pERK/tERK ratios, with OXT neurons showing a larger increase than non-OXT neurons. **c**, Spatial distribution of the most strongly activated OXT (upper) and non-OXT (lower) neurons in the PO and PT. To be classified as highly active, pERK/tERK ratios must exceed the threshold at which <3% of OXT neurons in control conditions would be considered active. The same threshold is applied to non-OXT neurons. To account for differences in neuron number due to varying dataset sizes, 500 randomly sampled OXT neurons and 1,000 randomly sampled non-OXT neurons are displayed per experimental group. **d**, Calcium imaging of OXT neurons in response to noxious stimuli. The same fish (*n* = 231 neurons from 7 independent fish) were exposed to electric shock (6 V cm⁻¹), mustard oil (25 μM, bath exposure), heat (peak temperature >37 °C) and taps (suprathreshold to elicit startle behavior). Raster plots show average calcium responses of all neurons tested, sorted by the strength of their shock responses. Neuron number is consistent across all raster plots, allowing for comparison across stimuli. Shock and tap responses were aligned using the onset of the stimulus, while mustard oil and heat signals were aligned to the maximum response within 60 s of stimulus delivery. Calcium traces show the average response across all neurons, and shading indicates the s.e.m. Red bars indicate the stimulus period. To quantify the spatial distribution of activated neurons, we set a threshold (integrated calcium signal value of 1; Supplementary Fig. 3) above which neurons were considered to be highly active. This method likely underestimates the extent of activation by these stimuli, since weakly activated neurons (for example, from tap stimuli) would be excluded.

As a diffusible stimulus that binds covalently to TRPA1 (ref. 28), mustard oil is difficult to deliver in a spatiotemporally precise way. To explore the dynamic relationship between TRPA1 channel activation, OXT signaling and behavior, we took advantage of a small molecule, optovin^{29,30}, which can be photoconverted into a TRPA1 agonist in the presence of ultraviolet light. After the light is switched off, optovin reverts to an inactive state within seconds^{29,30}. By immersing larvae in optovin and stimulating the tail with brief pulses of 405 nm of light, we could activate TRPA1 in a spatially and temporally controlled manner (Fig. 3a).

Optovin-based TRPA1 stimulation consistently elicited tail bends, which were significantly higher in frequency, velocity and magnitude than the average movement elicited by light when the fish were in dimethylsulfoxide (DMSO) (Fig. 3b; Supplementary Video 1). These large-angle tail bends were also observed after mustard oil and noxious heat stimulation, which suggests that they are likely a nocifensive response (Supplementary Fig. 3c). The similarity between optovin-evoked and other forms of nocifensive behavior suggested that we could use this approach to further characterize OXT-mediated sensorimotor processing.

OXT neuron activity is induced by TRPA1 stimulation and correlates with nocifensive behavior. Whereas the mammalian hypothalamus contains thousands of OXT neurons, the larval zebrafish has fewer than 100 (55.0 ± 0.76 (OXT_{PO}), 12.9 ± 0.34 (OXT_{PT}), mean of 83 fish; Supplementary Fig. 2a,b), making it possible to record the activity of a large fraction of the population and to correlate the activity of each neuron with behavioral output. Since a substantial subset (~70%) of OXT_{PO} neurons, and occasionally a few OXT_{PT} neurons, are labeled by *Tg(oxt:Gal4;UAS:GCaMP6s)* (38.6 ± 3.00 neurons (OXT_{PO}), 0.79 ± 0.30 neurons (OXT_{PT}), mean \pm s.e.m. of 14 fish), we were able to combine volumetric two-photon calcium imaging, optovin-mediated TRPA1 stimulation and behavioral recordings to simultaneously monitor

population-wide OXT neuron activity and nocifensive behavior in real time (Fig. 3a).

While we only occasionally observed OXT neuron activation following stimulation with ultraviolet light when the fish were in DMSO, OXT neurons showed strong and synchronous responses to TRPA1 activation that varied with stimulus intensity and correlated with larger and longer-lasting tail movements (Fig. 3c). In contrast, ultraviolet light stimulation of the fish in DMSO was associated with a smaller calcium response and lower amplitude tail movement that was similar across light intensities (Fig. 3d). OXT neuron activity was also higher during spontaneous large-angle bouts, which suggests that OXT neurons are potentially involved in driving motor behaviors in other contexts (Fig. 3c,d). The rise in calcium activity on average appeared to slightly precede tail movements, a phenomenon that was most obvious during spontaneous events (Fig. 3d).

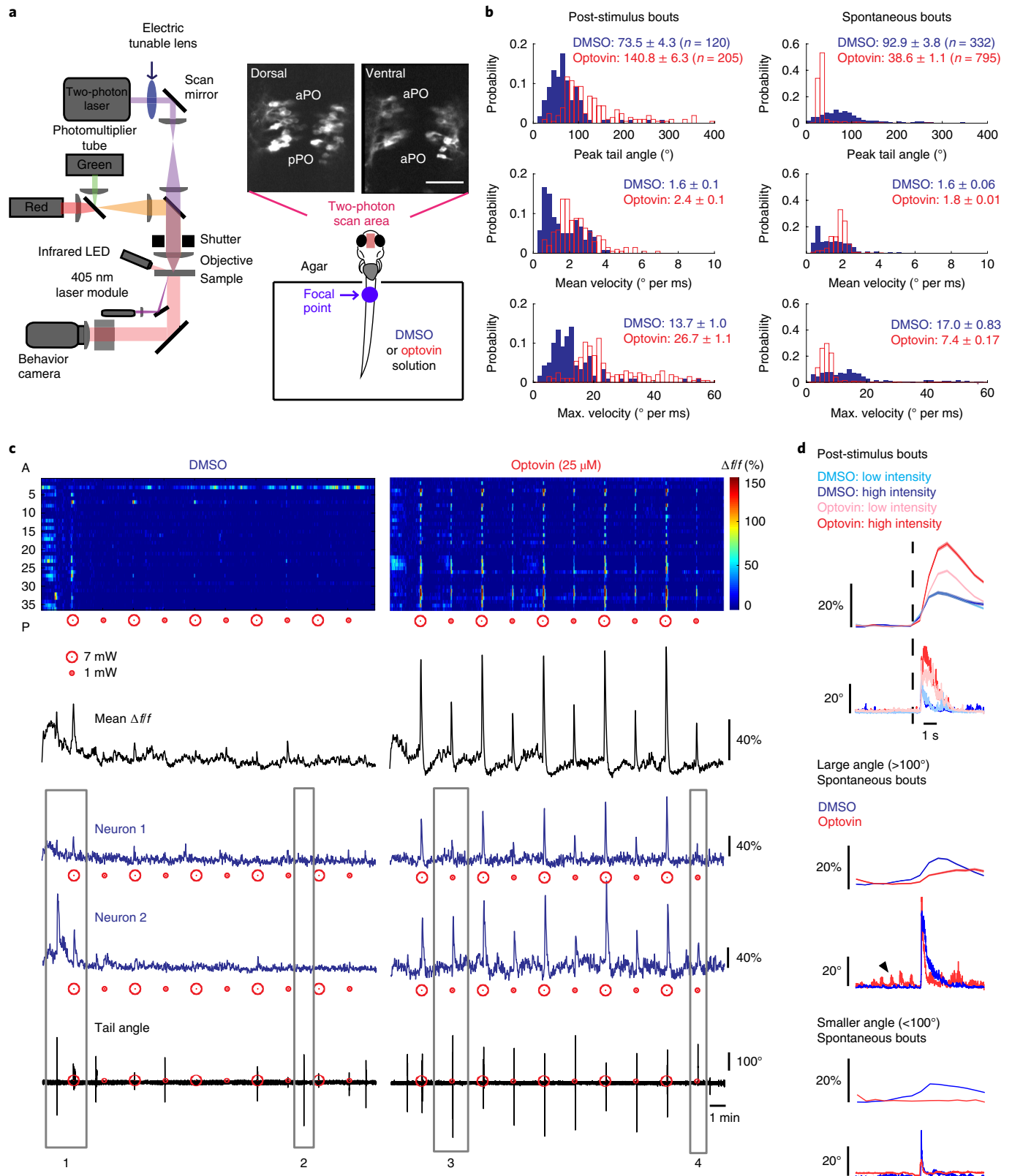
However, there were also instances of spontaneous large-angle tail bends that were not obviously accompanied by OXT activity, and other instances in which OXT activity was not correlated with strong behavioral output (Fig. 3c). This diversity of responses in individual cells corresponded not only to TRPA1 stimulus and motor responses but also to spontaneous and stimulus-induced movements that occurred in DMSO (Fig. 3c).

Diversity and distribution of OXT sensorimotor responses to TRPA1 activation. To further probe the diversity of sensorimotor representations within these cells, we generated stimulus and motor regressors and used them to classify neurons into distinct functional types on the basis of their degree of correlation with the stimulus and/or behavior³¹. The stimulus regressor varied with the absolute ultraviolet light intensities presented to the fish in both DMSO and optovin. To distinguish stimulus-locked and spontaneous motor activity in the OXT population, we generated two types of motor regressors: one that reflected stimulus-locked motor output (motor_{stim.} regressor) and another that reflected spontaneous

Fig. 3 | OXT neuron activity correlates with TRPA1 stimulus and nocifensive behavior. **a**, Schematic of TRPA1 stimulation setup for volumetric calcium imaging. An electrically tunable lens was used for volumetric imaging of the OXT population, labeled by *Tg(oxt:Gal4;UAS:GCaMP6s)*. Two to three z-volumes were sufficient to span the entire population. Images show ventral and dorsal views in a representative fish. Scale bar, 50 μ m. Fish were stimulated using a 405-nm laser focused on the bottom (ventral side) of the anterior part of the tail. **b**, Probability distribution of peak (i.e., maximum) cumulative tail angles, maximum and mean swim velocity of extracted bouts that occurred either post-stimulus (that is, within 5 s of stimulus) or spontaneously (all other times). Ultraviolet light stimulation in optovin (that is, TRPA1 stimulation) significantly increased the number of bouts ($n_{\text{bouts}} = 120$ DMSO/205 optovin, peak tail angle magnitude ($***P = 1.8 \times 10^{-21}$), mean tail velocity ($***P = 8.2 \times 10^{-10}$) and maximum tail velocity ($***P = 6.6 \times 10^{-25}$) in optovin compared to DMSO. While spontaneous swim frequency ($n_{\text{bouts}} = 332$ DMSO and 795 optovin) was also increased in optovin, there was a significant reduction in peak angle magnitude ($***P = 6.5 \times 10^{-69}$) and maximum velocity ($***P = 1.3 \times 10^{-46}$) during spontaneous events, and a small increase in mean velocity ($***P = 4.1 \times 10^{-16}$) when bouts were pooled across fish (two-sided Wilcoxon rank-sum test). Statistics by fish (post-stimulus): $***P = 4.9 \times 10^{-4}$ (frequency), $***P = 2.4 \times 10^{-4}$ (peak angle), $***P = 2.4 \times 10^{-4}$ (max. velocity), $***P = 4.9 \times 10^{-4}$ (mean velocity). Statistics by fish (non-stimulus bouts): $P = 0.35$ (frequency), $P = 0.052$ (peak angle), $P = 0.57$ (mean velocity), $***P = 4.9 \times 10^{-4}$ (max. velocity decrease), $n = 14$ fish, two-sided Wilcoxon signed-rank test. **c**, Volumetric imaging of an example *Tg(oxt:Gal4;UAS:GCaMP6s)* fish. Raster plots show $\Delta f/f$ activity traces for all visible OXT neurons ($n = 38$ neurons, 2 non-overlapping z-planes) for the entire experiment (10 ultraviolet light stimuli of 100 ms duration alternating between two intensities (1 mW and 7 mW), 120 s ISI). In this plot, neurons are sorted along the A-P axis. The same neurons were visually identified in both the DMSO and optovin conditions. Lower: average $\Delta f/f$ for all neurons and simultaneously recorded tail angle traces. Two example neurons are shown: neuron 1 appears strongly correlated with the TRPA1 stimulus and neuron 2 shows activity more consistent with behavioral correlation. Four gray boxes provide examples of: (1) spontaneous and post-ultraviolet light stimulus activation of neuron 2 that correlates with motor output; (2) spontaneous large-angle motor output that is not reflected by activity of either neuron; (3) large-angle tail bend that occurs during weak TRPA1 (optovin + ultraviolet light) stimulus, with neuron 1 showing weak activation, and neuron 2 showing strong activation; (4) weak behavioral output corresponding to weak TRPA1 stimulus, whereby both neurons 1 and 2 similarly show weak activation. **d**, Bout-triggered averages of calcium activity ($\Delta f/f$) and tail angle ($^\circ$) in DMSO and optovin for either the first bouts post-stimulation (1 mW and 7 mW light intensity; upper panels, $n = 2,516$ (DMSO; 1 mW), 3,312 (optovin; 1 mW), 2,123 (DMSO; 7 mW), 2,648 (optovin; 7 mW) calcium traces corresponding to 61, 84, 53 and 67 detected bouts from 14 fish), spontaneous bouts with peak tail angle magnitude above 100° (middle panels, $n = 3,959$ (DMSO) and 1,460 (optovin) calcium traces corresponding to 103 and 34 detected bouts from 14 fish) or spontaneous bouts with peak tail angle magnitude below 100° (lower panels, $n = 9,595$ (DMSO) and 26,112 (optovin) calcium traces corresponding to 229 and 761 detected bouts from 14 fish). Black arrowhead identifies small-amplitude tail twitches that occasionally occur in the optovin condition after repeated ultraviolet light stimulation. These twitches are usually indistinguishable from noise and did not affect correlational analyses. Scale bars represent either 20% $\Delta f/f$ or 20° tail angle for calcium and tail angle traces, respectively. Shading for calcium traces (where visible) represent the s.e.m. Since the peak tail angle magnitudes per bout were measured within a 5-s window from bout onset, the average peak magnitude may not correspond to the peak magnitude of individual bouts. Broken black line represents stimulus onset.

locomotion occurring in the absence of the stimulus (motor regressor). In both DMSO and optovin, stimulus and motor output (that is, motor_{stim.}) were only moderately correlated ($r=0.36 \pm 0.03$ in DMSO, 0.67 ± 0.04 in optovin; Supplementary Fig. 4a), which suggests that there was sufficient variability to probe both sensory

and motor components of the OXT circuit. We then correlated the activities of all OXT neurons ($n=552$ from 14 fish) to the three stimulus and motor regressors for both DMSO and optovin conditions (six regressors in total) to probe the distribution of sensorimotor representations in noxious and non-noxious contexts (Fig. 4a).



As predicted, many more neurons showed significantly stronger correlation with the stimulus and behavior in optovin (that is, TRPA1 activation) compared to DMSO (ultraviolet light alone), which is reflected by a right-shift in the distribution of correlation coefficients (Fig. 4b). In contrast, the correlation of OXT neuron activity with spontaneous behavior was slightly reduced in optovin versus DMSO, which is likely because of an increase in small-amplitude forward swims ('tail twitches') that occurred in some fish after repeated stimulation with optovin (see Fig. 3d for examples).

Across a range of thresholds, the proportion of cells that showed stimulus or motor correlations in optovin was higher than in DMSO or for spontaneous movements, confirming that OXT neurons predominantly respond to TRPA1 activation (Fig. 4c). At a stringent threshold of $r=0.35$, which was based on an estimate of spurious correlations (Supplementary Fig. 4b,c), we found that 39% of OXT neurons had activity that correlated with the stimulus regressor in optovin, and a lower, partially overlapping proportion (29%) was correlated with post-stimulus motor activity (that is, motor_{stim.} regressor; Fig. 4d). In optovin, the activity of stimulus-correlated neurons tended to parallel stimulus intensity, whereas motor_{stim.}-related neurons had more variable activity in response to both strong and weak stimuli, and thus might be encoding motor behavior (Fig. 4a,f).

In contrast, only 10% of all neurons showed stimulus correlation in DMSO, while 6% showed stimulus-related motor activity, which is consistent with the observation that most ultraviolet light stimulations in DMSO resulted in much weaker behavioral responses compared to those in optovin. We also did not observe ultraviolet light-related activity in all animals (Fig. 4e). Of the small fraction of OXT neurons that were responsive to ultraviolet light in DMSO, the response magnitude appeared to be much larger but less sensitive to stimulus intensity (Fig. 4f). Since ultraviolet light is also a mildly aversive and potentially damaging stimulus in zebrafish³², the observation of ultraviolet-light-induced responses is consistent with a broader role for OXT neurons in encoding negative inputs. We also found cells that were active both in DMSO and optovin (Fig. 4d; Supplementary Fig. 4c). It is possible that these cells continue to encode the ultraviolet light stimulus in optovin or are multimodal cells that are also tuned to TRPA1 stimulation.

Notably, some OXT neurons had activities that were correlated with spontaneous tail bends, which suggests that OXT neuron activity is not only simply evoked by the ultraviolet light or TRPA1 stimulus but may also have an independent motor function. It is

possible that a subset of these 'spontaneous' movements reflect behavioral responses to the heat of two-photon laser stimulation, since they often occurred at the onset of two-photon laser scanning (Fig. 3c). Consistent with this idea, a majority (60%) of OXT neurons that fired in correlation with spontaneous movements in DMSO or optovin were also activated by TRPA1 stimulation (Fig. 4d; Supplementary Fig. 4c).

Similar to our pERK and other calcium imaging results, TRPA1-stimulus- or motor-related neurons were highly intermingled and distributed throughout the population (Fig. 4g), with a slight enrichment of TRPA1-stimulus-related neurons in the aPO relative to motor-related and ultraviolet-light-responsive neurons. Since we strictly controlled for the area of stimulation, it is unlikely that this distributed pattern is a function of receptive field location.

To determine whether nociceptive responses are unique to OXT neurons or are a general property of cells in the PO or PT, we repeated our TRPA1 stimulation and in vivo imaging experiments in a pan-neuronal GCaMP6s line (*Tg[HuC:GCaMP6s]*) co-expressing *Tg[oxf:Gal4;UAS:nfsb-mCherry]* to define OXT and non-OXT populations, and compared the activities of these groups in the same fields of view (Supplementary Figs. 5 and 6; $n=13$ fish). Similar to our pERK results, OXT neurons were more strongly activated by TRPA1 stimulation than were non-OXT neurons, whereas activity observed during spontaneous movements and ultraviolet light stimulation were more similar between the two groups (Supplementary Figs. 5 and 6).

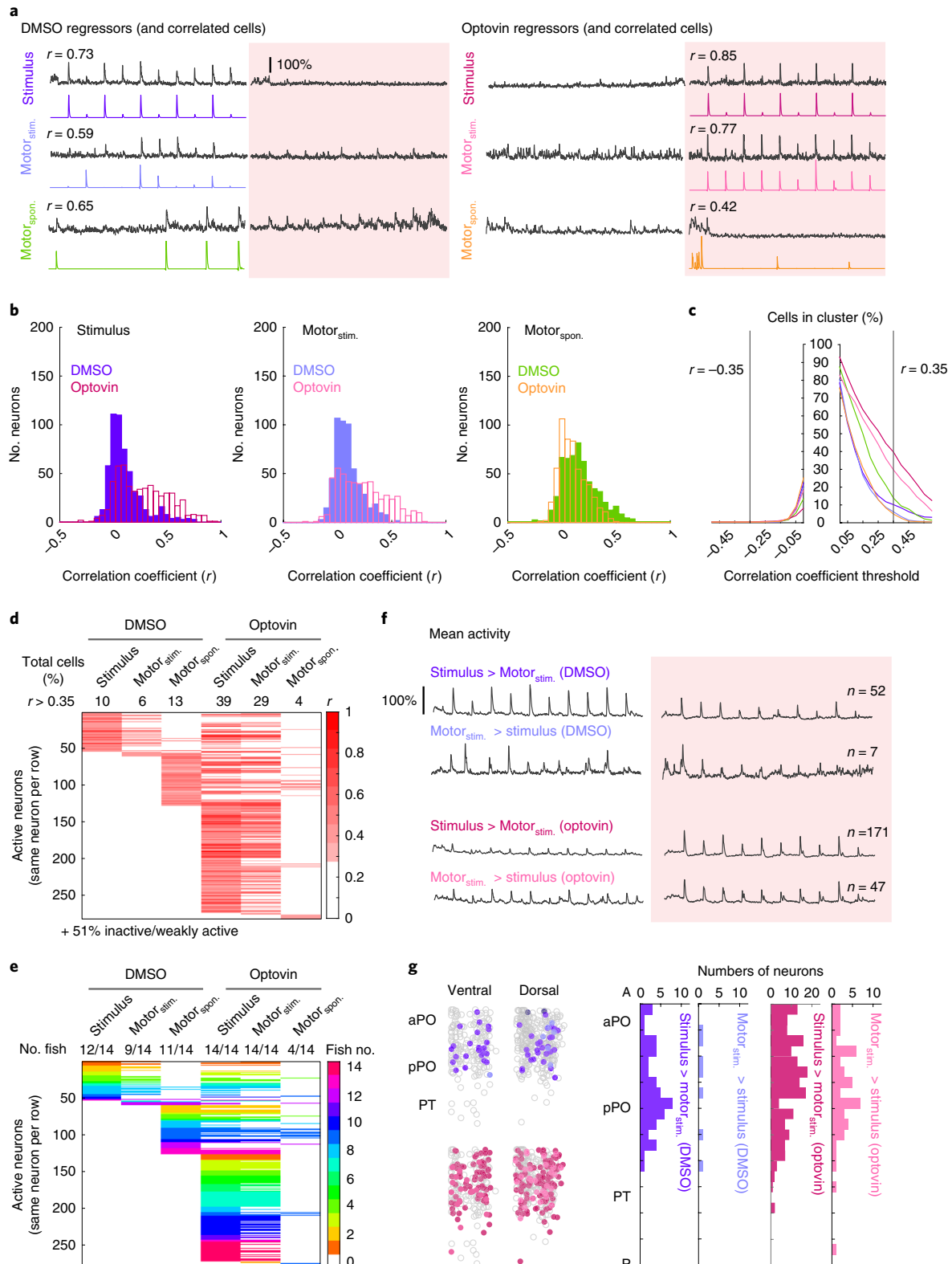
In summary, OXT neurons comprise a highly diverse and functionally heterogeneous population of cells with variable roles in the sensory and motor components of nociceptive and aversive signaling. A significant subset shows activity locked to defensive behavior, which raises the possibility that OXT may contribute to behaviors caused by TRPA1 receptor activation.

Optogenetic activation of OXT neurons drives large-angle tail bends. To determine whether OXT neurons play a role in driving locomotor responses to noxious stimuli, we expressed channelrhodopsin (ChR2) in OXT neurons using *Tg[oxf:Gal4;UAS:ChR2-EYFP]* fish (Fig. 5a). Focusing spatially restricted blue light onto ChR2-positive OXT_{PO} neurons evoked strong swimming behavior (Fig. 5a–c; Supplementary Video 2). Behavior could also be elicited by stimulating free-swimming eyeless fish (Fig. 5i,j), but not sibling controls that lacked ChR2 expression (Fig. 5d,e), thus demonstrating that the behavior was not visually evoked. However, stimulus

Fig. 4 | Diversity of sensorimotor encoding by OXT neurons. **a**, Regressors for six neuron classes that correspond to the stimulus, stimulus-locked behavior (motor_{stim.}) and spontaneous (motor_{spont.}) behavior in both DMSO and optovin, and $\Delta f/f$ traces from an example neuron that shows strong correlation with each regressor. The response of a neuron in DMSO and optovin (shaded pink area) are shown. Note that each neuron may correlate with more than one regressor. **b**, Histograms showing Pearson's correlation coefficients (r values) of all neurons to all six regressors. Many neurons show higher correlation to the stimulus and motor_{stim.} regressors in optovin than in DMSO (that is, TRPA1-responsive neurons). Mean increase in stimulus correlation = 0.17, $P=8.15 \times 10^{-41}$; mean increase in motor_{stim.} correlation = 0.13, $P=1.29 \times 10^{-23}$; mean increase in motor_{spont.} correlation = -0.07, $P=8.82 \times 10^{-15}$, one-sided Wilcoxon rank-sum test. **c**, The percentage of cells that would be classified into each cluster as a function of the cut-off r value used. At all thresholds, the largest clusters would correspond to neurons showing high correlation to the stimulus and motor_{stim.} regressors in optovin (that is, TRPA1-responsive neurons). Colors correspond to neuronal subtypes shown in **a** and **b**. We set our cut-off at a stringent threshold of $r=0.35$ (Supplementary Fig. 4b). **d**, Classification of neurons into six different response types. Each row corresponds to a single neuron, and the correlation coefficients to the corresponding regressors are represented by color intensity. A total of 49% of neurons belong to at least one of the clusters. Neurons that belong to none of the clusters ('inactive/weakly active neurons' (279/552 neurons), 51%) are not shown. Numbers shown above each column correspond to the percentage of neurons belonging to each category. **e**, Clustered neurons color-coded by individual fish highlight both the similarities across fish (for example, optovin stimulus and motor_{stim.}-correlated neurons) as well as individual variability. Numbers shown above correspond to the fraction of all fish in which neurons belonging to each category were identified. All fish had stimulus- and motor-correlated neurons in optovin trials. However, not all fish tested had stimulus or motor_{stim.}-correlated neurons in DMSO. **f**, Mean calcium activity of neurons with either higher or lower stimulus (versus motor) correlations in DMSO or optovin. Given that stimulus and motor_{stim.} regressors are themselves correlated, many of these neurons in fact are correlated with both regressors. However, strongly stimulus-correlated neurons show higher intensity tuning, whereas strongly motor-correlated neurons have more varied activity patterns due to variation in motor behavior. **g**, Left: two-dimensional spatial distribution of neuronal classes described in **f**. Right: histogram of neurons from each class found at each position along the A–P axis. For visualization purposes, the scale (that is, the number of neurons) for optovin stimulus-correlated neurons is different from that of other groups.

durations on the order of seconds were required to achieve a high probability of response (Fig. 5b–e), and the mean latency to behavior onset was relatively long (1.8 ± 0.13 s for 5 s of stimulus; Fig. 5f,g,k). Response frequencies and latencies were also highly variable (Fig. 5c,f,g,k). Because we used high light intensities (6 mW mm^{-2}) that were sufficient to activate other neurons at much shorter latencies (Supplementary Fig. 7a), it is unlikely that the long lag and

variability of OXT-evoked behavior is due to insufficient illumination. Since even in stable transgenic fish we rarely observed ChR2 labeling in more than 25 OXT_{PO} neurons per animal (that is, $\sim 50\%$ of the population; Supplementary Fig. 7d,e), and only a subset of these neurons might encode motor output, it is possible that a longer stimulation period is required to recruit sufficient neurons to drive behavior. Furthermore, OXT-containing vesicles might only



be released following prolonged stimulation, which might, in a more naturalistic scenario, be necessary for reducing response latencies^{5,21,33}. Using mosaic labeling, we found that the probability and frequency of optogenetically induced swimming strongly correlated with the number of OXT_{PO} neurons expressing ChR2 (Supplementary Fig. 7d,e). Notably, we were able to optogenetically induce swimming even in fish that had few or no pituitary projections (Supplementary Fig. 7e). Thus, it is likely that this behavior is mediated, at least in part, by parvocellular OXT neuron projections to the hindbrain and spinal cord.

Similar to TRPA1 receptor activation, tail bends induced by OXT neuron stimulation were greater in magnitude and kinematically distinct from C-bends induced by taps, acoustic startle or optogenetic activation of somatosensory neurons (Fig. 5h; Supplementary Figs. 7a–c and 8). Thus, instead of specifically activating classical predator escape reflex circuits that are identical to those driven by milder aversive stimuli¹⁸, OXT might modulate a distinct or partially overlapping network that promotes a faster and larger-angle motor output in response to noxious stimuli.

Role of the neuropeptide OXT in driving large-angle tail bends.

As in mammals^{34,35}, we found that zebrafish OXT neurons co-express glutamatergic markers (Fig. 6a), thus raising the question of the relative contributions of OXT itself versus other neurotransmitters in driving defensive behavior. To address this question, we first tested whether OXT applied directly to the exposed hindbrain and spinal cord was sufficient to drive large-angle tail bends. Fish were transected at the midbrain–hindbrain boundary, and all tissue anterior to the hindbrain, including the OXT neurons, was removed. Beginning at about 5 min after bath application of OXT, we observed a large burst of swimming activity comprised mostly of large-angle tail bends (Fig. 6b–d; Supplementary Videos 3 and 4). These results suggest that the peptide OXT can act directly on hindbrain–spinal circuitry and is sufficient, even in a reduced preparation, to drive behavior that resembles nocifensive responses.

We next asked whether OXT was necessary for ChR2-induced behavior. To that end, we used the clustered regularly interspaced

short palindromic repeats (CRISPR)–Cas9 system to generate OXT-null (*oxT^{-/-}*) mutant zebrafish, and identified a 575-bp deletion that was predicted to be a null allele (Fig. 6e). We then compared the effect of optogenetically stimulating OXT neurons in OXT-null mutants and their heterozygous siblings (Fig. 6f; Supplementary Fig. 9a,b,d). While the absence of OXT did not completely abolish ChR2-evoked swimming behavior, it significantly reduced its probability, frequency and response latency. There were no observable differences between wild-type and heterozygous OXT mutants (Supplementary Fig. 9c). Thus, the absence of OXT attenuates the efficacy of OXT neurons in driving locomotion.

Taken together, these results suggest that although the peptide OXT is sufficient to drive large-angle tail bends, OXT neurons possess functionally redundant mechanisms, likely involving co-expressed neurotransmitters, which can partially compensate for the absence of OXT. We propose glutamate as the most likely candidate for supplying this excitatory locomotor drive³⁶.

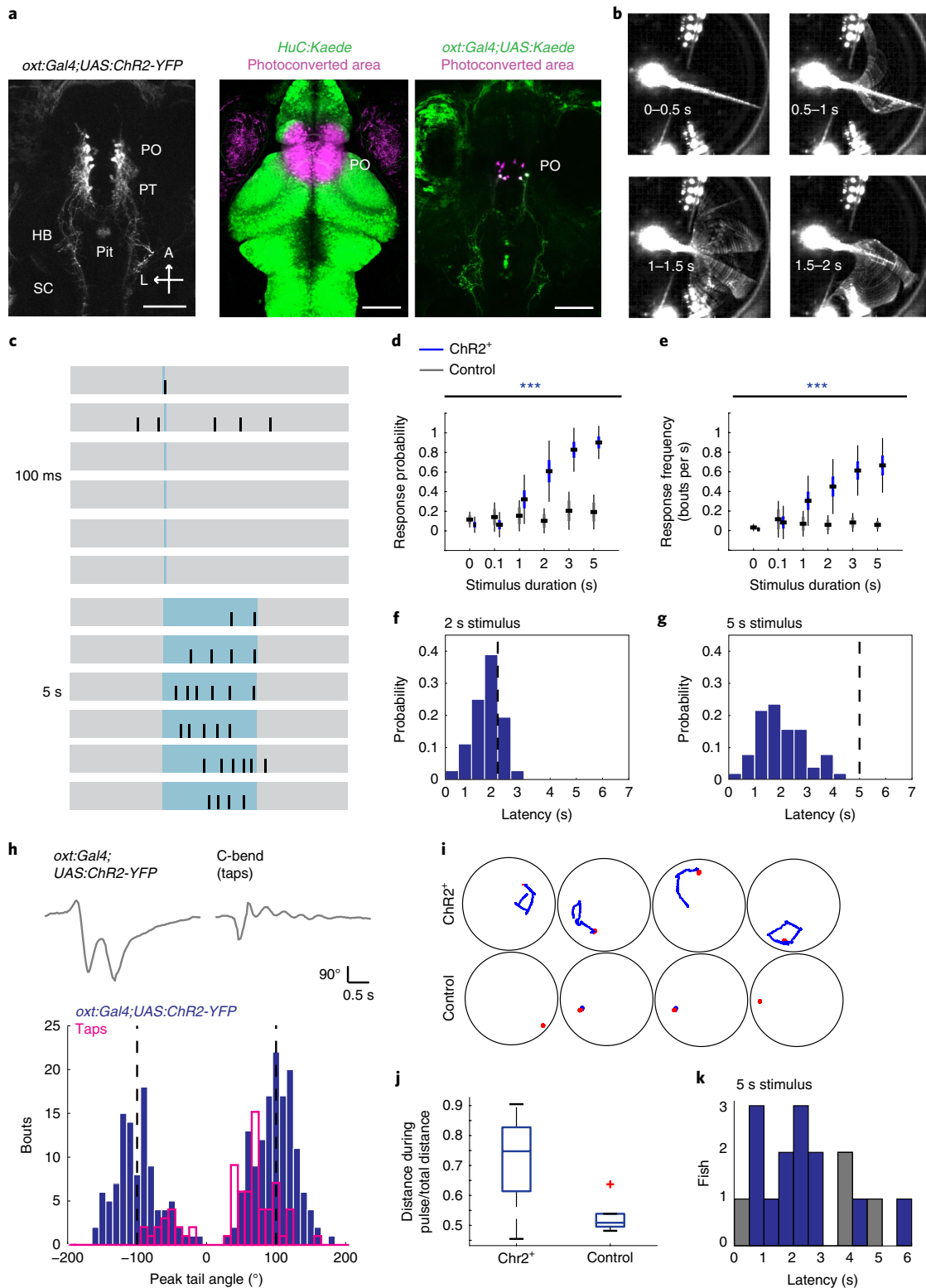
Brainstem reticulospinal neurons are downstream targets of TRPA1 and OXT neuron activation.

To identify the neuronal targets by which OXT elicits defensive behavior we focused on the reticulospinal system³⁷, a highly stereotyped population of approximately 250 spinally projecting motor command neurons that we found to be densely innervated by *Tg(oxT:GFP)*-expressing axons (Fig. 7a). Calcium imaging of the reticulospinal array during either ChR2 or optovin stimulation allowed us to identify cells that are activated downstream of OXT neuron activation or nociceptor signaling. We found that both TRPA1 activation and *Tg(oxT:Gal4; UAS:ChR2-EYFP)* stimulation activated a common subset of these cells, including the M-cell and several other premotor targets (RoM2, RoM3, RoL3, MiV1 and MiV2; Fig. 7a–d). Evoked calcium signals in these neurons reliably preceded fictive motor bursts recorded by electromyography (EMG) (Fig. 7b–d). The probability of activation for each reticulospinal cell type was strikingly similar between TRPA1 stimulation and optogenetic OXT activation, which suggests that there is overlap between these pathways.

Fig. 5 | Optogenetic activation of OXT neurons drives large-angle tail bends. **a**, Maximum intensity projection of *Tg(oxT:Gal4;UAS:ChR2-YFP)* fish shows strong PO expression and projections to the pituitary, hindbrain and spinal cord (left). Photo-conversion of *Tg(HuC:Kaede)* (center) and *Tg(oxT:Gal4;UAS:Kaede)* (right) fish marks the region that is exposed to light during optogenetic stimulation. Scale bar, 100 μ m. These experiments were repeated on three fish each, with similar results obtained. **b**, Maximum intensity projection images showing the behavior of a representative *Tg(oxT:Gal4;UAS:ChR2-YFP)* fish during different time periods after blue light onset. These experiments were repeated on more than 50 fish, with similar results obtained. **c**, Responses of a single fish to 100-ms and 5-s stimuli and showing variability in response frequency and latency. Each vertical black line represents a detected swim bout. Each stimulation period is highlighted in blue. Only the first 100-ms stimulus produced a response. These experiments were repeated on more than 50 fish, with similar results obtained. **d**, Response probability of *Tg(oxT:Gal4;UAS:ChR2-YFP)* fish (blue) increases with stimulus duration and is significantly higher than for controls lacking ChR2-YFP expression ($F_{(1,240)} = 139.48$, $***P = 1.12 \times 10^{-25}$, $n = 29$ and 13, two-way ANOVA). There was a significant interaction between genotypes and stimulus duration ($***P = 1.38 \times 10^{-22}$). Data were pooled over multiple clutches. A single pulse of the stipulated duration was delivered for each 30-s trial. Center black lines represent the means; boxes represent 1 s.d.; range, 95% confidence intervals. **e**, Normalized response frequency for the same group of fish increases with stimulus duration and is significantly higher than for controls ($F_{(1,240)} = 106.81$, $***P = 5.99 \times 10^{-21}$, $n = 29$ and 13, two-way ANOVA). There was a significant interaction between genotypes and stimulus duration ($***P = 8.56 \times 10^{-14}$). Center black lines represent the means; boxes represent 1 s.d.; range, 95% confidence intervals. **f**, Histogram of response latencies in head-embedded fish for a 2-s light stimulus (mean latency = 1.37 ± 0.08 s, $n = 36$ responses from 10 fish). Broken black lines indicate the end of blue light stimulation. Data are from a single clutch. **g**, Histogram of response latencies in the same group of head-embedded fish for a 5-s light stimulus (mean latency = 1.80 ± 0.13 s, $n = 51$ responses from 10 fish). **h**, Upper: example of tail bend kinematics (cumulative angle versus time) elicited by *Tg(oxT:Gal4;UAS:ChR2-YFP)* stimulation (left) compared with a typical escape response elicited by a strong vibrational-acoustic tap stimulus (right). Lower: peak tail angles per bout elicited by photoactivation of OXT neurons (blue) versus a strong vibrational-acoustic tap stimulus in a different group of fish (magenta). The mean tail angle is significantly larger for *Tg(oxT:Gal4;UAS:ChR2-YFP)* stimulation ($100.11 \pm 1.93^\circ$, $n = 246$ bouts from 10 fish, 5-s stimulus) than for taps ($68.96 \pm 3.09^\circ$, $n = 75$ bouts from 10 fish, $***P = 2.06 \times 10^{-9}$, two-sided Wilcoxon rank-sum test). Broken black lines indicate 100° , which is the mean peak tail angle from *Tg(oxT:Gal4;UAS:ChR2-YFP)* stimulation. **i**, ChR2-driven free-swimming behavior in blind fish. Example swim trajectories from representative ChR2-positive fish and controls. Red, pre-pulse swim trajectory; blue, post-pulse swim trajectory. **j**, ChR2-positive fish showed a significant increase in distance traveled during the light pulse (normalized to total distance traveled). ChR2: 0.716 ± 0.037 cm, controls: 0.53 ± 0.02 cm, $n = 14$ and 6, $*P = 0.015$, two-sided Wilcoxon rank-sum test. Box plots show the median, interquartile range and entire data range excluding outliers. Outlier is depicted by a red cross. **k**, Histogram of mean latencies per fish for ChR2-positive (blue, 2.36 ± 0.41 s) and control (gray, 3.2 ± 0.79 s) fish. Since many control fish did not swim at all, fewer data points are depicted for that group.

The M-cell is a crucial component of zebrafish escape circuitry^{18,38,39}. While the kinematic differences between TRPA1- or OXT-driven behaviors and other forms of escape suggested that there is differential reliance on downstream targets, our observation that one of the two M-cells were activated during ~50% of optovin and ChR2 trials (Fig. 7c) led us to ask whether they might play a similarly important role in shaping the properties of nocifensive

behavior. To that end, we bilaterally ablated both M-cells and measured behavioral responses to both TRPA1 and optogenetic OXT stimulation (Fig. 7e). The majority of behavioral parameters, including response probability, frequency, maximum bend angle, velocity and duration, were unaffected by M-cell ablation relative to sham-ablated controls (Fig. 7f; Supplementary Fig. 10). The only exception was behavioral latency, which was significantly increased for



optogenetically evoked but not optovin-evoked swimming (Fig. 7g; Supplementary Fig. 10; ChR2: mean increase = $+360.9 \pm 104.7$ ms, $*P = 0.03$; optovin: mean increase = -192.7 ms ± 76.5 ms, $P = 0.062$ (not significant (NS))). The differential effects on latency might reflect a lower degree of complexity in the neuronal signals elicited by ChR2 activation versus more naturalistic sensory stimuli. Overall, we conclude that the characteristic features of TRPA1-induced and OXT-induced behavior do not absolutely require the M-cell and are instead relayed to the spinal cord through the parallel activation of multiple reticulospinal targets.

Loss of OXT function attenuates behavioral responses to TRPA1 stimulation. Finally, to determine whether the OXT circuit was necessary for the implementation of nociceptive behavior, we used optovin to photochemically activate TRPA1 receptors in free-swimming larval zebrafish (Fig. 8a). As with restrained fish, TRPA1 stimulation strongly increased locomotor output by eliciting large-angle tail bends (Fig. 8b; Supplementary Videos 5 and 6). Due to limitations of our behavioral setup, we were not always able to perfectly resolve tail angles in those experiments, and thus used velocity changes as a more reliable behavioral metric.

We chemogenetically ablated OXT neurons in transgenic *Tg(oxt:Gal4;UAS:nitroreductase-mCherry)* fish by treatment with metronidazole (MTZ), a pro-drug that is enzymatically converted into a toxic product by nitroreductase to cause cell-specific ablation (Supplementary Fig. 11). Since *Tg(oxt:Gal4;UAS:nitroreductase-mCherry)* has variegated expression, this manipulation likely only ablates about 50–75% of the OXT population. Despite this caveat, partial ablation with MTZ (starting from 5 days post fertilization (d.p.f.)) also significantly reduced responses to TRPA1 stimulation relative to MTZ-treated control siblings lacking nitroreductase (Fig. 8c). There were no differences in light responses while in DMSO. In optovin, the median post-stimulation increase in swim speed was 35% lower in OXT neuron-ablated fish than for control siblings. Furthermore, ablation of OXT neurons did not affect baseline swim kinematics, which suggests that the effects of our manipulation were specific to nociceptive behavior (Fig. 8d).

We next asked whether genetic deletion of OXT (which attenuated OXT neuron-evoked locomotion (Fig. 6f; Supplementary Fig. 9a,b)) similarly reduced TRPA1-activation-induced behavior. We compared the behavioral responses of *oxt*^{-/-} mutants and their heterozygous siblings. Loss of OXT significantly attenuated light-evoked behaviors in optovin-treated fish (Fig. 8e), while no differences between genetic groups were observed in DMSO control

trials. In optovin, the median post-stimulation increase in swim speed was 38% lower in *oxt*^{-/-} mutants compared with heterozygous siblings (Fig. 8c), which is similar to the effect observed with OXT neuron ablation. Deletion of OXT also did not affect baseline swim kinematics, which suggests that the reduction in TRPA1-induced behavior was not due to a gross locomotor deficit (Fig. 8f). Taken together, these experiments demonstrate that OXT neurons contribute to driving the behavioral response to noxious stimuli.

Discussion

Using in vivo imaging of OXT population activity in zebrafish, we describe a multimodal neuromodulatory circuit that is involved in the sensorimotor transformation of nociceptive signals. A large and distributed fraction of hypothalamic OXT cells respond strongly to noxious inputs, including TRPA1 stimulation, and more weakly to other aversive stimuli. While some neurons are tuned specifically to sensory stimuli, others display behaviorally correlated activities, which together with gain-of-function and loss-of-function experiments implicate OXT in the generation of nociception-triggered motor output via the activation of brainstem premotor targets. Our results strongly support a conserved role for OXT in nociceptive processing and suggest diverse functions for OXT circuits in both the integration of sensory input and the generation of defensive locomotor responses.

Extensive activation of OXT neurons by noxious and other aversive stimuli. While previous mammalian studies have identified small, ostensibly specialized subpopulations of OXT neurons that may be involved in pain or fear processing^{4,5,10}, it has been unclear whether these subgroups are unique or ubiquitous. Here, through population-level activity recordings in behaving zebrafish, we show that a large percentage OXT neurons, likely spanning both parvocellular and magnocellular types, acutely respond to noxious stimuli.

The extent of OXT activation by a particular aversive stimulus appears to scale with the potential for damage. Notably, OXT neurons responded to aversive but non-nociceptive ‘startle’ stimuli, such as taps and ultraviolet light flashes, but to a lesser degree than for TRPA1 activation or noxious heat. Interestingly, the magnitude and extent of the OXT signals elicited by non-noxious stimuli varied dramatically between animals, suggesting that there is potential modulation by other factors such as prior exposure to noxious stimuli, contextual cues or internal state.

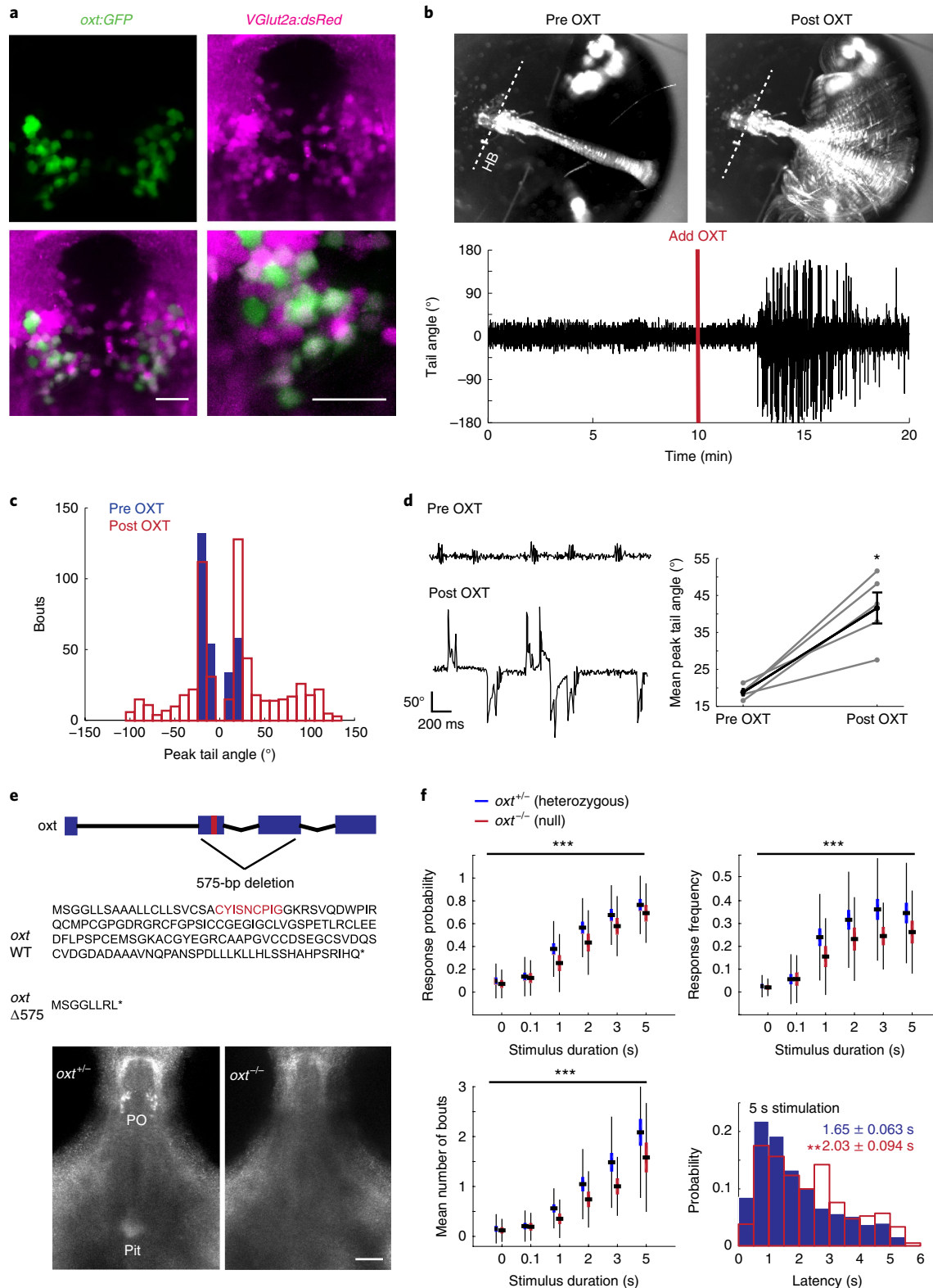
It is likely that OXT acts in concert with other closely apposed cell types, such as corticotropin-releasing factor- or arginine-vasotocin-expressing neurons^{14,35,36,40}, which have similarly been implicated in

Fig. 6 | Role of OXT neuropeptide in driving large-angle tail bends. **a**, Maximum intensity projections show *Tg(oxt:GFP)* neurons (green) overlapping with glutamate-expressing neurons labeled by *Tg(VGlu2a:dsRed)* (magenta). Lower-right image shows a higher magnification view. Scale bar, 20 μ m. The experiment was repeated on eight fish, with similar results obtained. **b**, Upper: maximum intensity projection images of a tethered fish in a reduced preparation from a 5-min interval before and after the addition of 5 μ M OXT. More anterior tissue was removed from the hindbrain. Lower: example trace showing tail angle versus time in this reduced preparation. The experiment was repeated on five fish, with similar results obtained. **c**, Distribution of peak tail angles per bout for a 10-min period before and after addition of OXT, for the fish shown in **b**. Peak tail angles are significantly higher after addition of OXT. Before: $16.57 \pm 0.17^\circ$, $n = 278$ detected bouts; after: $42.49 \pm 1.31^\circ$, $n = 576$ detected bouts, $***P = 2.27 \times 10^{-61}$, two-sided Wilcoxon rank-sum test. **d**, Left: representative tail angle traces showing pre OXT and post OXT behavior. Right: Peak tail angles are higher in the 10 min after addition of OXT than in the 10 min before addition ($*P = 0.0312$, $n = 5$ fish, one-sided Wilcoxon signed-rank test). **e**, Upper: schematic showing the zebrafish *oxt* gene. Exons 2 and 3, which include the sequence coding for the OXT peptide (red), are deleted in the *oxt* mutants. Predicted amino acid sequences for the products of the wild-type (WT) *oxt* gene and the *oxt* mutant allele are shown in the lower panel, with mutated amino acids in bold. Lower: antibody staining against OXT confirms the absence of the peptide in homozygous *oxt*^{-/-} (null) mutants. Scale bar, 50 μ m. Faint neuropil visible in *oxt*^{-/-} fish is due to background staining. The experiment was repeated on four heterozygous and three null mutants, with similar results obtained. **f**, Response probability, frequency and the number of responses per optogenetic stimulus are reduced in *oxt*^{-/-} mutants. Data shown are aggregated over multiple clutches of fish. Examples of data from individual clutches are shown in Supplementary Fig. 9. Difference in response probability: $F_{(1,846)} = 21.98$, $***P = 3.22 \times 10^{-6}$, normalized frequency: $F_{(1,846)} = 26.90$, $***P = 2.68 \times 10^{-7}$, number of bouts: $F_{(1,846)} = 26.49$, $***P = 3.30 \times 10^{-7}$, $n = 92$ heterozygous and 51 null fish, two-way ANOVA. For response frequency, there is a significant interaction between genotype and stimulus duration ($*P = 0.0207$). Center black lines represent the mean; boxes represent 1 s.d.; range, 95% confidence intervals. Lower right: response latencies during a 5-s stimulus are significantly longer for null mutants (mean = 2.03 ± 0.094 s) than for their heterozygous (mean = 1.65 ± 0.063 s) siblings. $**$ Adjusted $P = 0.0013$, $n = 422/212$ bouts, two-sided Wilcoxon rank-sum test, Bonferroni corrected.

pain and stress behaviors. In both zebrafish and mammals, OXT may form part of a larger paraventricular 'stress response' network, which together with other brain regions such as the locus coeruleus, area postrema and caudal hypothalamus, coordinates defensive behavior against noxious and other threatening stimuli^{41,42}.

OXT neurons drive defensive locomotion via the reticulospinal circuitry. A small number of previous studies have suggested

a locomotor role for OXT using pharmacological manipulation of reduced preparations. However, the functional relevance of such observations was unknown or speculated to be related to reproductive behaviors^{43–45}. Our finding that OXT (and OXT neuron activation) can drive large-angle tail bends directly links the in vivo activity of OXT neurons to defensive locomotion. These behaviors are kinematically distinct from the startle responses that are elicited by the threat of predation, which suggests an evolution



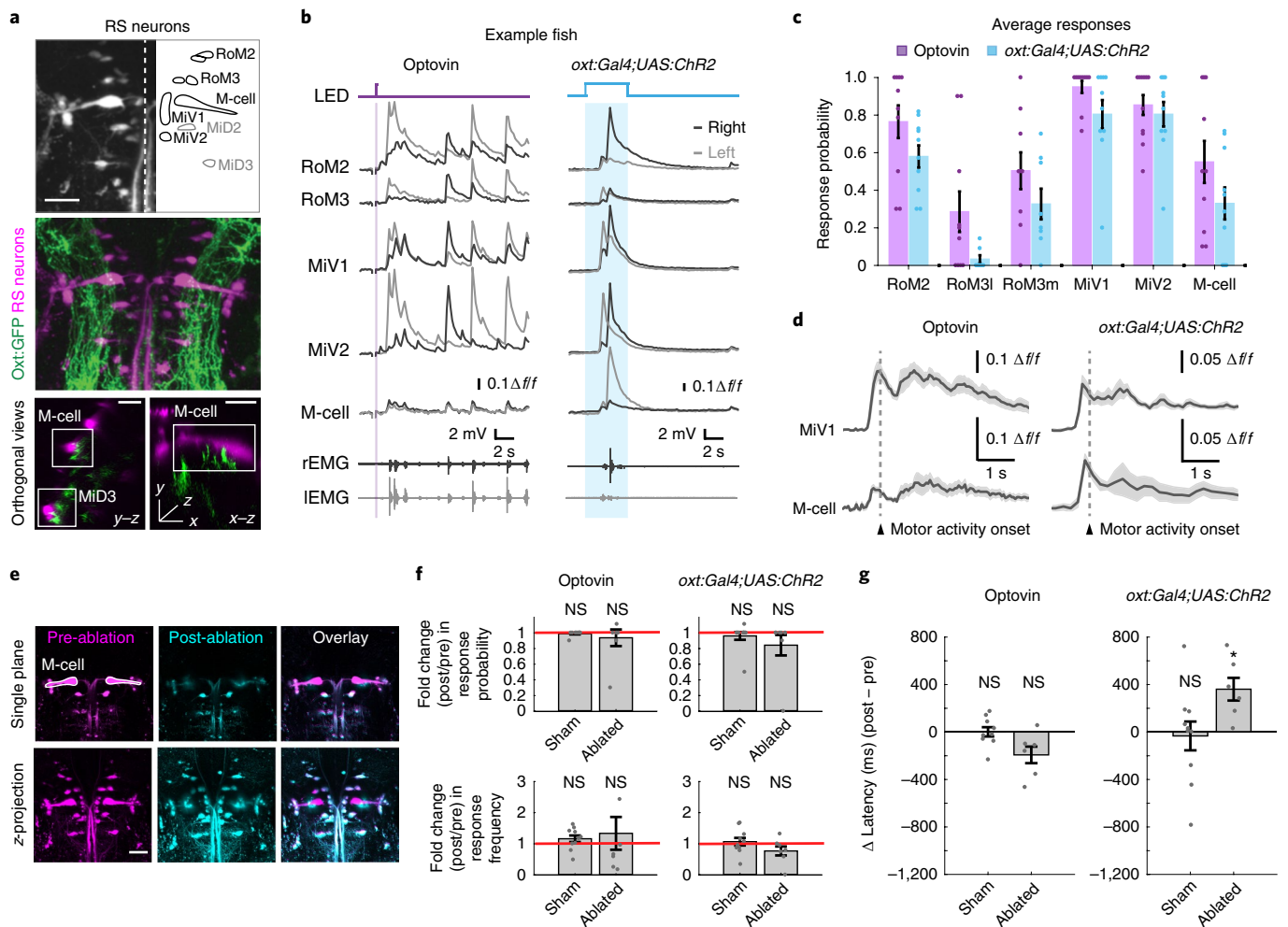


Fig. 7 | TRPA1 and OXT activation drive brainstem reticulospinal neurons. **a**, Axons of OXT neurons (green) project to the hindbrain and colocalize with reticulospinal (RS) neurons (magenta). Upper: the RS cell types where activity was measured are highlighted (black). MiD2 and MiD3 (gray) are M-cell homologs that also respond to optovin and ChR2 stimulation, but were not consistently labeled by backfilling and hence excluded from analysis. Lower: orthogonal views of OXT axon proximity to RS cell types, including the M-cell. Scale bars, 20 μ m. The experiment was repeated on 12 fish, with similar results obtained. **b**, Example traces showing calcium activity evoked in reticulospinal neurons by TRPA1 stimulation (optovin) or optogenetic activation of OXT neurons (*Tg(oxt:Gal4;UAS:ChR2-YFP)*), along with simultaneous EMG recordings. Pulses of ultraviolet (410 nm, 100 ms) or blue (480 nm, 5 s) light were used to activate optovin and ChR2, respectively. Black traces represent neuronal and EMG activity from the right side of the fish and gray traces represent activity from the left. The optovin and ChR2 experiments were repeated on six and five fish, respectively, with similar results obtained. **c**, Response probabilities of reticulospinal neurons during optovin stimulation or ChR2-mediated OXT neuron activation. A 5% $\Delta f/f$ increase is set as the threshold for activation. Bar plots show the mean \pm s.e.m. Sample sizes for the optovin experiment (cell number/fish number): RoM2 (10/6), RoM3I (10/6), RoM3m (10/6), MiV1 (10/6), MiV2 (11/6), M-cell (10/6). For the ChR2 experiment (cell number/fish number): RoM2 (10/5), RoM3I (7/4), RoM3m (8/4), MiV1 (10/5), MiV2 (10/5), M-cell (10/5). There is no significant difference between the two groups for any cell type (RoM2, $P=0.08$; RoM3I, $P=0.10$; RoM3m, $P=0.26$; MiV1, $P=0.08$; MiV2, $P=0.61$; M-cell, $P=0.18$; two-sided Wilcoxon rank-sum test). **d**, Calcium responses of MiV1 and the M-cell aligned to the onset of the first swim bout after optovin stimulation or ChR2-mediated OXT neuron activation (mean \pm s.e.m.). Shading indicates the s.e.m. Scale bar, 20 μ m. The experiment was repeated on 14 fish, with similar results obtained. **e**, M-cell fluorescence from an example fish pre- and post-bilateral ablation. Upper: single plane; lower: maximum intensity projection. Scale bar, 20 μ m. The experiment was repeated on 14 fish, with similar results obtained. **f**, Fold change in probability (upper) and frequency (lower) of response in sham controls and M-cell ablated fish, for both optovin-mediated TRPA1 stimulation (left; $n=10$ fish (sham) and 7 fish (ablated), two-sided Wilcoxon signed-rank test) and optogenetic OXT activation (right; $n=10$ fish (sham) and 7 fish (ablated)). The response probabilities and frequencies were unchanged in most animals, except for some outliers (optovin (sham, ablated): $P_{\text{probability}}=1, 1$; $P_{\text{frequency}}=0.27, 0.69$; ChR2 (sham, ablated): $P_{\text{probability}}=1, 0.5$; $P_{\text{frequency}}=0.87, 0.22$; two-sided Wilcoxon signed-rank test comparing post- to pre-ablation values per fish). Bar plots show the mean \pm s.e.m. Fish that had a baseline response probability of <0.5 were subsequently excluded from kinematic analysis. **g**, Mean difference in latency of response (ms) of sham controls and M-cell-ablated fish. When quantified across fish, there was a non-significant reduction in response latencies for TRPA1 stimulation (left; mean increase = $+1.5 \pm 41.5$ ms (sham), -192.7 ± 76.5 ms (ablated), $n=9/6$ (sham/ablated), $P=0.91/0.06$ (sham/ablated)) and a significant post-ablation increase in response latencies for optogenetic OXT activation (right; mean increase = -33.1 ± 127.9 ms (sham), $+360.9 \pm 104.7$ ms (ablated), $n=10/6$ (sham/ablated), $P=0.85, *P=0.03$ (sham, ablated), two-sided Wilcoxon signed-rank test comparing post- to pre-ablation latencies per fish). Bar plots show the mean \pm s.e.m. See also Supplementary Fig. 10 for additional measured kinematic parameters and statistical analyses.

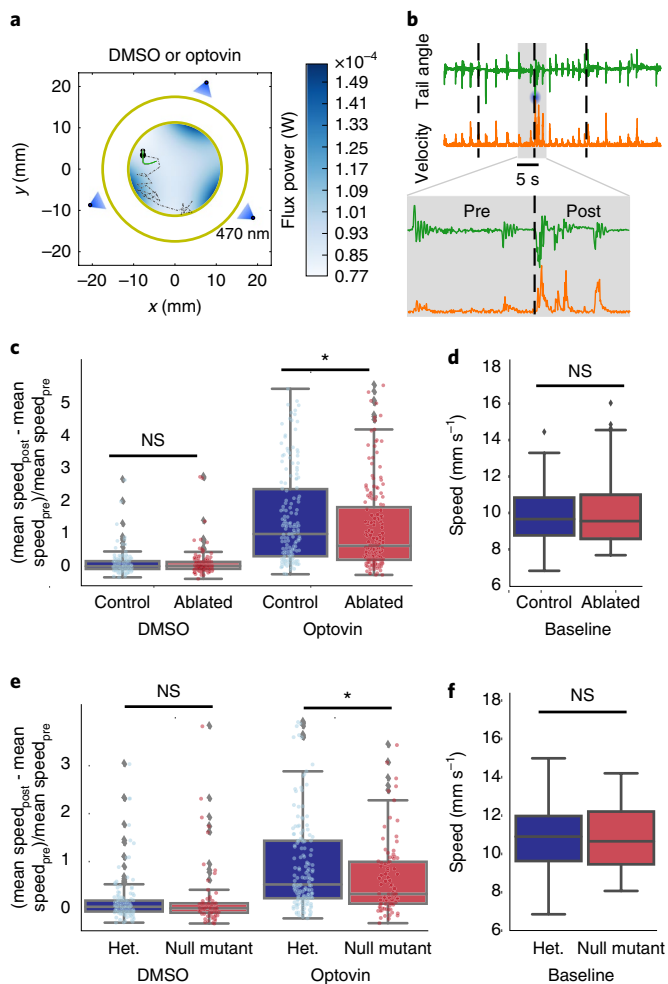


Fig. 8 | Loss of OXT function attenuates behavioral responses to TRPA1 activation. **a**, Schematic of the free-swimming TRPA1 stimulation behavioral setup. **b**, Upper: representative example of the head velocity (mm s^{-1}) and cumulative tail angle ($^{\circ}$) of a fish before and after light stimulation (blue circle) in optovin solution. All of the response parameters were computed in the 5 s pre- and post-stimulus time windows. Lower: higher magnification images of the gray highlighted area. **c**, Chemical-genetic ablation of OXT neurons reduces responses to TRPA1 stimulation. While MTZ-mediated ablation of OXT neurons did not affect behavior in DMSO ($P=0.93$, $n_{\text{control}}=141$ stimulations from 44 fish, $n_{\text{ablated}}=137$ stimulations from 44 fish, two-sided Wilcoxon rank-sum test), in optovin, the response of ablated fish was 35% lower than for MTZ-treated sibling controls ($*P=0.024$, $n_{\text{control}}=162$ stimulations from 44 fish, $n_{\text{ablated}}=175$ stimulations from 44 fish). Box plots in **c–e** show the median, interquartile range and entire data range excluding outliers. Outliers are depicted by gray diamonds. **d**, Comparison of baseline swim speeds between MTZ-treated control and ablated fish ($P=0.77$, two-sided Wilcoxon rank-sum test). The baseline kinematics were calculated for the 3-min period before the first stimulation in the DMSO condition. **e**, Genetic deletion of *oxt* reduces responses to TRPA1 stimulation. While light flashes were equally ineffective at eliciting responses for both genotypes in DMSO ($P=0.29$, $n_{\text{het.}}=145$ stimulations from 45 fish, $n_{\text{null}}=69$ stimulations from 26 fish, two-sided Wilcoxon rank-sum test), in optovin the response of the mutants was 38% lower than for heterozygous (Het.) controls ($*P=0.015$, $n_{\text{het.}}=160$ stimulations from 45 fish, $n_{\text{null}}=89$ stimulations from 26 fish). **f**, Comparison of baseline swim speeds between heterozygous and null mutants ($P=0.92$, two-sided Wilcoxon rank-sum test). The baseline kinematics were calculated for the 3-min period before the first stimulation in the DMSO condition.

of distinct mechanisms for escaping the potential for harm (that is, predator approach) versus actual physical harm, similar to what has been proposed in mammals². Such distinctions appear to be mediated by a differential reliance on hindbrain premotor neurons. While the M-cell is considered to be an essential component of the startle response, it responds less reliably than other premotor cells to TRPA1 or OXT stimulation, and its ablation has few consistent effects on evoked behaviors. Thus, we infer that the contribution of M-cells to the unique characteristics of OXT- and TRPA1-evoked swimming is minimal or redundant with other OXT targets.

Our data also suggest that the ability of OXT neurons to recruit reticulospinal targets relies on the simultaneous release of both OXT peptide and other neurotransmitters, such as glutamate. Although OXT itself is sufficient to induce large-angle tail bends, genetic deletion of OXT only partially impairs optogenetically induced locomotion and nociceptive behavioral responses. While the purpose of such functional redundancy is still unknown, the OXT peptide has previously been shown to facilitate to synaptic transmission, sharpen spike timing and increase the robustness of spike transmission, and thus may be important for modulating the latency, precision or intensity of defensive locomotor behaviors⁴⁶. OXT co-release could also exert more sustained effects on the hindbrain–spinal circuitry through sensitization and synaptic plasticity⁴⁷. Additional approaches such as patch-clamp recordings of identified locomotor targets and cell-specific genetic perturbation of glutamate biosynthesis will be required to confirm this hypothesis.

OXT circuit function across evolution. OXT is most often characterized as a pain- and fear-reducing molecule that attenuates the behavioral responses to threats, yet it has also been shown to enhance fear, pain and defensive responses in rodents and humans^{6,8,9,48}. Our data show that these ‘behavior-activating’ effects of OXT should be considered alongside the anxiolytic, antinociceptive and anti-inflammatory functions that have been demonstrated in other studies⁴. While OXT is sufficient to drive defensive locomotion in zebrafish, it could simultaneously be playing an anxiolytic or analgesic role. For example, a recent paper⁴⁹ showed that direct and persistent activation of TRPV1 nociceptors by OXT leads to receptor desensitization and analgesia over the long term. Indeed, our discovery of both sensory- and motor-related cell types that span both magnocellular and parvocellular OXT populations is suggestive of multiple integrative pathways being triggered in parallel.

The locomotion-enhancing effects of OXT in mammalian spinal preparations, overall conservation of OXT neuroanatomy and expression of OXT receptors within mammalian spinal circuits⁵⁰ all suggest that the role of OXT in motivating defensive behaviors could be conserved in other vertebrates, even if precise motor targets and behavioral output differ between species¹. Overall, our study highlights how neural pathway dissection in the larval zebrafish model can be used to characterize sensorimotor transformations within neuromodulatory populations, and complement mammalian studies in demonstrating the sufficiency of hypothalamic activation for the execution of fundamental defensive behaviors.

Online content

Any methods, additional references, Nature Research reporting summaries, source data, statements of code and data availability and associated accession codes are available at <https://doi.org/10.1038/s41593-019-0452-x>.

Received: 7 December 2017; Accepted: 18 June 2019;

Published online: 29 July 2019

References

1. LeDoux, J. Rethinking the emotional brain. *Neuron* **73**, 653–676 (2012).

2. Gross, C. T. & Canteras, N. S. The many paths to fear. *Nat. Rev. Neurosci.* **13**, 651–658 (2012).
3. Dubin, A. E. & Patapoutian, A. Nociceptors: the sensors of the pain pathway. *J. Clin. Invest.* **120**, 3760–3772 (2010).
4. Eliava, M. et al. A new population of parvocellular oxytocin neurons controlling magnocellular neuron activity and inflammatory pain processing. *Neuron* **89**, 1291–1304 (2016).
5. Knobloch, H. S. et al. Evoked axonal oxytocin release in the central amygdala attenuates fear response. *Neuron* **73**, 553–566 (2012).
6. Poisbeau, P., Grinevich, V. & Charlet, A. in *Behavioral Pharmacology of Neuropeptides: Oxytocin* Vol. 35 (eds Hurlmann, R. & Grinevich, V.) 193–211 (Springer, 2017).
7. Rojas-Piloni, G. et al. Oxytocin, but not vasopressin, modulates nociceptive responses in dorsal horn neurons. *Neurosci. Lett.* **476**, 32–35 (2010).
8. Grillon, C. et al. Oxytocin increases anxiety to unpredictable threat. *Mol. Psychiatry* **18**, 958–960 (2013).
9. Striepens, N. et al. Oxytocin facilitates protective responses to aversive social stimuli in males. *Proc. Natl Acad. Sci. USA* **109**, 18144–18149 (2012).
10. Knobloch, H. S. & Grinevich, V. Evolution of oxytocin pathways in the brain of vertebrates. *Front. Behav. Neurosci.* **8**, 31 (2014).
11. Wirrcer, E. et al. Homeodomain protein Otp affects developmental neuropeptide switching in oxytocin neurons associated with a long-term effect on social behavior. *eLife* **6**, e22170 (2017).
12. Herget, U., Gutierrez-Triana, J. A., Salazar Thula, O., Knerr, B. & Ryu, S. Single-cell reconstruction of oxytocinergic neurons reveals separate hypophysiotropic and encephalotropic subtypes in larval zebrafish. *ENEURO*.0278-16.2016 (2017).
13. Coffey, C. M. et al. Novel oxytocin gene expression in the hindbrain is induced by alcohol exposure: transgenic zebrafish enable visualization of sensitive neurons. *PLoS One* **8**, e53991 (2013).
14. Herget, U., Wolf, A., Wullmann, M. F. & Ryu, S. Molecular neuroanatomy and chemoarchitecture of the neurosecretory preoptic-hypothalamic area in zebrafish larvae. *J. Comp. Neurol.* **522**, 1542–1564 (2014).
15. Swanson, L. W. & Sawchenko, P. E. Paraventricular nucleus: a site for the integration of neuroendocrine and autonomic mechanisms. *Neuroendocrinology* **31**, 410–417 (1980).
16. Sawchenko, P. E. & Swanson, L. W. Immunohistochemical identification of neurons in the paraventricular nucleus of the hypothalamus that project to the medulla or to the spinal cord in the rat. *J. Comp. Neurol.* **205**, 260–272 (1982).
17. Saito, D., Komatsuda, M. & Urano, A. Functional organization of preoptic vasotocin and isotocin neurons in the brain of rainbow trout: central and neurohypophysial projections of single neurons. *Neuroscience* **124**, 973–984 (2004).
18. Korn, H. & Faber, D. S. The Mauthner cell half a century later: a neurobiological model for decision-making? *Neuron* **47**, 13–28 (2005).
19. Randlett, O. et al. Whole-brain activity mapping onto a zebrafish brain atlas. *Nat. Methods* **12**, 1039–1046 (2015).
20. Tsukamoto, G. & Adachi, A. Neural responses of rat area postrema to stimuli producing nausea. *J. Auton. Nerv. Syst.* **49**, 55–60 (1994).
21. Ludwig, M. & Leng, G. Dendritic peptide release and peptide-dependent behaviours. *Nat. Rev. Neurosci.* **7**, 126–136 (2006).
22. Swanson, L. W. & Sawchenko, P. E. Hypothalamic integration: organization of the paraventricular and supraoptic nuclei. *Annu. Rev. Neurosci.* **6**, 269–324 (1983).
23. Prober, D. A. et al. Zebrafish TRPA1 channels are required for chemosensation but not for thermosensation or mechanosensory hair cell function. *J. Neurosci.* **28**, 10102–10110 (2008).
24. Venkatchalam, K., Luo, J. & Montell, C. Evolutionarily conserved, multitasking TRP channels: lessons from worms and flies. *Handb. Exp. Pharmacol.* **223**, 937–962 (2014).
25. Bautista, D. M., Pellegrino, M. & Tsunozaki, M. TRPA1: a gatekeeper for inflammation. *Annu. Rev. Physiol.* **75**, 181–200 (2013).
26. Gau, P. et al. The zebrafish ortholog of TRPV1 is required for heat-induced locomotion. *J. Neurosci.* **33**, 5249–5260 (2013).
27. Patapoutian, A., Tate, S. & Woolf, C. J. Transient receptor potential channels: targeting pain at the source. *Nat. Rev. Drug Discov.* **8**, 55–68 (2009).
28. Macpherson, L. J. et al. Noxious compounds activate TRPA1 ion channels through covalent modification of cysteines. *Nature* **445**, 541–545 (2007).
29. Kokel, D. et al. Photochemical activation of TRPA1 channels in neurons and animals. *Nat. Chem. Biol.* **9**, 257–263 (2013).
30. Lam, P.-Y. et al. A high-conductance chemo-optogenetic system based on the vertebrate channel Trpa1b. *Sci. Rep.* **7**, 11839 (2017).
31. Orger, M. B. & Portugues, R. Correlating whole brain neural activity with behavior in head-fixed larval zebrafish. *Methods Mol. Biol.* **1451**, 307–320 (2016).
32. Guggiana-Nilo, D. A. & Engert, F. Properties of the visible light phototaxis and UV avoidance behaviors in the larval zebrafish. *Front. Behav. Neurosci.* **10**, 160 (2016).
33. van den Pol, A. N. Neuropeptide transmission in brain circuits. *Neuron* **76**, 98–115 (2012).
34. Hrabovszky, E. & Liposits, Z. Novel aspects of glutamatergic signalling in the neuroendocrine system. *J. Neuroendocrinol.* **20**, 743–751 (2008).
35. Stoop, R. Neuromodulation by oxytocin and vasopressin. *Neuron* **76**, 142–159 (2012).
36. Herget, U. & Ryu, S. Coexpression analysis of nine neuropeptides in the neurosecretory preoptic area of larval zebrafish. *Front. Neuroanat.* **9**, 2 (2015).
37. Fetcho, J. R., Higashijima, S. & McLean, D. L. Zebrafish and motor control over the last decade. *Brain Res. Rev.* **57**, 86–93 (2008).
38. Liu, K. S. & Fetcho, J. R. Laser ablations reveal functional relationships of segmental hindbrain neurons in zebrafish. *Neuron* **23**, 325–335 (1999).
39. O'Malley, D. M., Kao, Y. H. & Fetcho, J. R. Imaging the functional organization of zebrafish hindbrain segments during escape behaviors. *Neuron* **17**, 1145–1155 (1996).
40. Vom Berg-Maurer, C. M., Trivedi, C. A., Bollmann, J. H., De Marco, R. J. & Ryu, S. The severity of acute stress is represented by increased synchronous activity and recruitment of hypothalamic CRH neurons. *J. Neurosci.* **36**, 3350–3362 (2016).
41. Gutierrez-Triana, J. A., Herget, U., Lichtner, P., Castillo-Ramirez, L. A. & Ryu, S. A vertebrate-conserved cis-regulatory module for targeted expression in the main hypothalamic regulatory region for the stress response. *BMC Dev. Biol.* **14**, 41 (2014).
42. Amir-Zilberstein, L. et al. Homeodomain protein otp and activity-dependent splicing modulate neuronal adaptation to stress. *Neuron* **73**, 279–291 (2012).
43. Wagenaar, D. A., Hamilton, M. S., Huang, T., Kristan, W. B. & French, K. A. A hormone-activated central pattern generator for courtship. *Curr. Biol.* **20**, 487–495 (2010).
44. Pearson, S. A., Mouhate, A., Pittman, Q. J. & Whelan, P. J. Peptidergic activation of locomotor pattern generators in the neonatal spinal cord. *J. Neurosci.* **23**, 10154–10163 (2003).
45. Dose, F., Zanon, P., Coslovich, T. & Taccola, G. Nanomolar oxytocin synergizes with weak electrical afferent stimulation to activate the locomotor CpG of the rat spinal cord in vitro. *PLoS One* **9**, e92967 (2014).
46. Owen, S. F. et al. Oxytocin enhances hippocampal spike transmission by modulating fast-spiking interneurons. *Nature* **500**, 458–462 (2013).
47. Marlin, B. J. & Froemke, R. C. Oxytocin modulation of neural circuits for social behavior. *Dev. Neurobiol.* **77**, 169–189 (2017).
48. Guzmán, Y. F. et al. Fear-enhancing effects of septal oxytocin receptors. *Nat. Neurosci.* **16**, 1185–1187 (2013).
49. Nersesyan, Y. et al. Oxytocin modulates nociception as an agonist of pain-sensing TRPV1. *Cell Rep.* **21**, 1681–1691 (2017).
50. Reiter, M. K. et al. Localization of oxytocin binding sites in the thoracic and upper lumbar spinal cord of the adult and postnatal rat: a histoautoradiographic study. *Eur. J. Neurosci.* **6**, 98–104 (1994).

Acknowledgements

The authors thank E. Glasgow (Georgetown University) for providing the *Tg(oxl:GFP)* transgenic line and *oxl:GFP* plasmid, which we used to generate the *oxl:Gal4* line, L. O'Connell and H. Gainer (NINDS) for providing an OXT antibody and M. Manning (University of Toledo) for providing the pharmacological tools for preliminary experiments. The authors are especially grateful to D. Schoppik, M. Haesemeyer, D. Guggiana-Nilo and J. Yang for helping with preliminary experiments and to R. Portugues for sharing software. They also thank C.-T. Yang and M. Ahrens for sharing transgenic lines used in preliminary experiments and the Zebrafish International Resource Center (ZIRC) for providing the *Tg(UAS:nfsb-mCherry)* transgenic line. Support from S. Turney and the CBS imaging facility, as well as A. Viel and the NorthWest Undergraduate Teaching Laboratories at Harvard, were essential for the successful completion of many experiments. J. Miller, S. Zimmerman, K. Hurley and B. Hughes at Harvard, as well as the University of Utah Centralized Zebrafish Animal Resource (CZAR), provided invaluable fish care. Finally, the authors thank N. Uchida, W. Carlezon, R. Dorsky and C. Gregg for helpful discussions and comments. This work was supported by the Sloan Foundation (to A.D.D.), NIH grants R01-NS111067 (to A.D.D.), U01-NS090449 (to F.E.), R24-NS086601 (to F.E.), U19-NS104653 (to F.E., A.D.D. and S.K.), T32-HL007901 (to A.M.B.L.), T32-NS076067 (to S.L.-M.), F31-NS100412 (to J.P.B.), DP1-HD094764 (to A.E.S.), Simons Foundation grant SCGB 325207 (to F.E.), and NSF CAREER IOS-10043082 (to A.D.D.). C.L.W. was supported by the National Science Scholarship from the Agency for Science, Technology and Research (A*STAR), Singapore.

Author contributions

C.L.W., A.D.D. and F.E. conceived the project, with S.K., E.S. and M.N. providing critical advice and guidance. A.D.D. and F.E. supervised the project. C.L.W. designed and performed most of the experiments and analyzed most of the data. M.N. developed hardware and software for calcium imaging and behavioral experiments, designed and performed some experiments and analyzed the free-swimming behavioral data. W.-C.W. and S.L.-M. performed experiments and analyzed data. E.S., O.R., A.M.B.L. and E.G. performed experiments. J.P.B. developed software for behavioral analysis. I.H.B. developed the optogenetic stimulation setup and advised experiments. J.G. and C.L.W. generated the OXT CRISPR mutant. A.D.D. and C.L.W. generated the *Tg(oxl:Gal4)* line.

A.F.S. supervised J.G., O.R. and A.M.B.L. and advised the project. C.L.W. and A.D.D. wrote the manuscript with contribution from all the other authors.

Competing interests

The authors declare no competing interests.

Additional information

Supplementary information is available for this paper at <https://doi.org/10.1038/s41593-019-0452-x>.

Reprints and permissions information is available at www.nature.com/reprints.

Correspondence and requests for materials should be addressed to F.E. or A.D.D.

Peer review information: *Nature Neuroscience* thanks Alexandre Charlet and the other, anonymous, reviewer(s) for their contribution to the peer review of this work.

Publisher's note: Springer Nature remains neutral with regard to jurisdictional claims in published maps and institutional affiliations.

© The Author(s), under exclusive licence to Springer Nature America, Inc. 2019

Methods

Fish husbandry. Larvae and adults were raised under standard conditions and maintained on a 14:10 light:dark cycle at 28 °C. All protocols and procedures involving zebrafish were approved by the Harvard University, Faculty of Arts and Sciences Standing Committee on the Use of Animals in Research and Teaching (IACUC) and by the University of Utah IACUC. All larvae were raised either in facility water or embryo water (0.6 g Instant Ocean in 2 liters of reverse osmosis water, adding bicarbonate to pH 7.2) and fed with an excess of paramecia daily starting from 5 d.p.f. All experiments were performed between 6 and 8 d.p.f.

Transgenic lines. The following transgenic lines were used in the study:

*Tg(oxl:GFP)*¹³ (E. Glasgow, Georgetown University);
Tg(oxl:Gal4) [*Tg(oxl:gal4-vp16)*] (generated for this study by A.D.D., F.E. and C.L.W.);
Tg(HuC:GCaMP6s) [*Tg(elavl3:GCaMP6s)13203*]⁵¹ (F.E.);
*Tg(UAS:GCaMP6s)*⁵² (K. Kawakami, NIG, Japan);
*Tg(UAS-E1b:NTR-mCherry)*⁵³ (available from ZIRC); *Tg(Vglut2a:dsRed)*⁵⁴;
*Tg(UAS:ChR2-YFP)*⁵⁵ (generated by A.D.D. and F.E.); *Tg(UAS-E1b:Kaede)*⁵⁶;
*Tg(isl2b:Gal4)*⁵⁷.

All the above lines were maintained in the AB background. For imaging experiments requiring unpigmented fish, the *mitfa* (*nacre*) mutation was introduced to these transgenic lines.

The *Tg(oxl:gal4-vp16)* line (referred to as *Tg(oxl:Gal4)*) was generated by PCR amplifying the 1.7-kb *oxl* enhancer sequence as previously described¹³, incorporating attB1/B2 sites, and then inserting it into the Gateway pDONOR vector via BP reaction to make pENTR:1.7oxl. This entry clone was then LR reacted against pDest-Tol2:gal4-vp16 to create the expression construct. The resulting plasmid was co-injected into one-cell stage, *Tg(UAS:nfsbCherry)*-expressing embryos (AB background) at a concentration of 30 ng μl^{-1} with *Tol2* transposase mRNA at a concentration of 30 ng μl^{-1} . A single founder was selected based on high and uniform levels of expression. The degree of expression mediated by the *Tg(oxl:Gal4)* line is dependent on the specific UAS transgene used.

Generation of *oxl* mutant using the CRISPR–Cas9 method. Ten Cas9 target sites within the *oxl* open reading frame were chosen using CHOPCHOP⁵⁸ to generate short guide RNA (sgRNA) molecules for mutagenesis. The DNA sequences used to create these sgRNAs are shown below. Cas9 protein was mixed with all ten sgRNAs and injected into embryos at the one-cell stage⁵⁹. Clutches from outcrosses of these injected fish were screened by PCR using flanking primers and Sanger sequencing to identify a 575-bp deletion allele. Founders were outcrossed repeatedly to reduce the likelihood of unlinked, off-target mutations affecting the *oxl*^{-/-} genotype. Lack of *oxl* expression was confirmed by immunostaining with an anti-OXT antibody (Fig. 6). Mutant fish were genotyped using a three primer PCR-based strategy. This mutant can be obtained from A. Douglass (University of Utah).

The following CRISPR sgRNAs were used:

oxl_target1: GTCTGGAGGTCTGCTGTCCGCGG;
oxl_target2: TGGAGGTCTGCTGTCCGCGGCGG;
oxl_target3: TGGGGCCGAAACACGCTCCGCGG;
oxl_target4: AGAAACCCTGCGTGCCTGGAGG;
oxl_target5: GAGATGTCTGAAAGGCCTGCGG;
oxl_target6: TGGAAAGGCTGCGGTTATGAGG;
oxl_target7: TGTCTCAGAGGCTGCAGTGTGG;
oxl_target8: GGATTCTAGAGGGGTGTGCGTGG;
oxl_target9: GTGTCTGCTGTCCGTCTGCTCGG;
oxl_target10: GATGTAGCAGGCCGAGCAGACGG.

The following *oxl* genotyping primers were used:

oxl_flanking_PCR_F: CTCTTCTCCACAGTAATGTCTGG;
oxl_flanking_PCR_R: CTCCTGAGATGATGCACAGCTC;
oxl_genotyping_PCR_F: ACAAGACACAAACACTAAGTAAGCATG;
oxl_genotyping_PCR_deletionR: GGCAAGTCATTGTATAACAGTGGTTTG;
oxl_genotyping_PCR_wild-typeR: GGCAGTTGAGATGTAGCAGG.

Whole-brain MAP-mapping experimental protocol. Larvae (7 d.p.f.) were divided evenly into control and treatment groups in 85-mm dishes and exposed to experimental stimuli. The protocols for optomotor and aversive stimuli (taps, electric shock and heat) have been previously published¹⁹. They are as follows: (1) electric shock: ~3 V cm^{-1} , once every 10 s for 15 min; (2) taps: suprathreshold tap once every 10 s for 15 min; (3) mustard oil: 10 or 25 μM in 0.1% DMSO for 15 min; (4) heat: 37 °C water bath for 15 min. In the data shown in Fig. 2, the inter-stimulus interval (ISI) for shock and taps was increased to 30 s to reduce desensitization, and two different shock intensities were tested. We also added a 40 °C heat treatment (15 min). Other protocols remained identical.

For the food stimulus, paramecia were added to a dish of larvae that had been food-deprived for 2 h, while paramecia water was added to the control. For cocaine treatments, fish were exposed to 1 μM cocaine-HCL (Sigma) or solvent (water) control. After 45 min (cocaine) or 15 min (all other stimuli), larvae were funneled through a sieve and then quickly dropped into 4% paraformaldehyde (PFA), immunostained, imaged and analyzed as previously described¹⁹.

High resolution (0.8 × 0.8 × 2 μm voxel size) confocal images of individual brains were then acquired and registered to a reference brain (x , y and $z = 621$, 1,406 and 138 voxels, respectively). Registered images were then downsampled (x , y and $z = 300$, 679 and 80 voxels, respectively); 1.6, 1.6 and 3.5 μm voxel size), and statistical comparisons were made at each voxel by calculating a Z-score between treatment and control. To set a false discovery rate (FDR) threshold, pseudogroups were assembled containing an equal number of randomly assigned fish from control and treatment groups, and a Z-score was calculated as before. We then set a FDR threshold of 0.00005, indicating a 0.005% probability of finding a value greater than this threshold in the pseudogroup comparison. The Z-scores for the real data were then thresholded at this value of Z, and suprathreshold voxels were assigned an intensity equal to the difference in the median values of the groups.

Automated quantification of high-resolution pERK data. For quantification of pERK/total ERK (tERK) ratios in individual OXT neurons, pERK experiments were performed on dissected *Tg(oxl:GFP)* fish, mounted in glycerol ventral side up on glass slides. High-resolution, tricolor (GFP, pERK and tERK) images were acquired using a confocal microscope (Olympus FV1000), and cellular data were automatically extracted using custom Fiji (ImageJ)⁶⁰ and Matlab software that will be made available online (Supplementary Fig. 1; <https://www.github.com/carolinewee>). The process involves the following steps: (1) ImageJ: cropping and reducing images to a specific region of interest (ROI); in this case, spanning the entire OXT_{PG} and OXT_{PT} populations; (2) ImageJ: extracting individual particles (that is, cells) using either an inverted and processed tERK image or directly from the GFP channel; (3) Matlab: quantification of activity based on extracted pERK/tERK ratios from both OXT and non-OXT cells; (4) Matlab: normalization of pERK/tERK ratios (to the mean of control groups) and aggregation of data across multiple experiments to increase sample sizes. For Fig. 2c, we plotted cells that exceeded a threshold above which only 3% of OXT:GFP-positive cells in the control group would be considered active. The same threshold was then applied to non-OXT cells.

Immunohistochemistry (for MAP-mapping and anti-OXT immunostaining).

After 24 h of fixation with 4% PFA in PBS + 0.25% Triton (PBT), fish were washed in PBT, incubated in 150 mM Tris-HCl (pH 9) for 15 min at 70 °C, washed in PBT, permeabilized in 0.05% Trypsin-EDTA for 45 min on ice, washed in PBT, blocked in blocking solution (10% goat serum, 0.3% Triton) for at least 1 h and then incubated in primary and secondary antibodies for up to 3 days at 4 °C in blocking solution. In between the primary and secondary antibody treatments, fish were washed in PBT and blocked for 1 h. For higher-resolution images, fish were dissected 24 h post-fixation, not permeabilized in Trypsin-EDTA before staining and mounted in glycerol on glass slides.

For immunostaining against OXT, we used either a commercial rabbit anti-OXT (used in Fig. 6; AHP371, AbD Serotec (now Bio-Rad), 1:300) or a rabbit anti-OXT (used in Supplementary Fig. 2; VA10, 1:5,000)⁶¹ from H. Gainer's laboratory (NIH, Bethesda, USA). Rabbit anti-pERK and mouse anti-ERK (tERK) antibodies (Cell Signaling, no. 4370 and no. 4969) were both used at 1:500 dilution¹⁹. Secondary antibodies conjugated with Alexa Fluor dyes (Life Technologies) were diluted 1:500.

In situ hybridization assays. For in situ hybridization, brains were fixed in 4% PFA + 5% sucrose, dissected out and processed according to a previously published protocol⁶². An OXT probe was generated by PCR amplification from zebrafish complementary DNA with the primers CTCCGCAAGCTCTCGGTGTC (forward) and CTGCACTAATGTACAGTCAAGC (reverse), TA cloning the resulting product into pGEM-T and in vitro transcription (mMessage mMachine SP6, Thermo Fisher). Following development with a BCIP reagent, brains were mounted in glycerol and imaged using an Olympus (BX51WI) compound fluorescence microscope.

Calcium imaging by confocal microscopy. Larvae (7–8 d.p.f.) of the *mit1fa*^{-/-} (*nacre*) background expressing *Tg(oxl:Gal4;UAS:GCaMP6s)* were embedded in 1.5% agarose (6-cm dish) with their tails freed. They were imaged at 1 frame per second (f.p.s.) on an upright confocal microscope (Olympus FV1000). For all experiments, a single plane covering the largest number of OXT neurons was imaged. Taps were delivered by striking the imaging platform with a solenoid (Guardian Electric 28P-I-12D). Shocks (100 ms, 36 V) were delivered across a 6-cm dish (~6 V cm^{-1}) using a Grass stimulator, with the anode and cathode placed near the head and tail of the fish, respectively. Heat was delivered using a heating coil positioned close to the tail of the fish (4 V, ~2 A, ~2 Ω). A 10-s heat stimulus was presented, achieving noxious temperatures of ~37 °C (peak temperatures may be higher), following which the water temperature was allowed to cool naturally (~5 min to return to room temperature). After >5 min of heat presentation, mustard oil was pipetted into the dish to achieve a final concentration of 25 μM . Calcium activity was analyzed in similar way as for the two-photon data (see below). The maximum calcium response within 60 s of heat or mustard oil stimulus was used to quantify neural responses, whereas tap and shock responses were aligned based on stimulus onset.

Behavioral recordings were performed on separate fish using the same stimulation methods. Uniformly distributed points along the tail of the fish were

extracted online at 100 f.p.s. using custom LabVIEW software, and cumulative tail angles analyzed and plotted analyzed in Matlab.

Simultaneous two-photon calcium imaging and behavior during optovin stimulation. Larvae (7–8 d.p.f.) homozygous for the *mit1fa* (*nacre*) allele, expressing *Tg(oxt:Gal4;UAS:GCaMP6s)* or co-expressing *Tg(oxt:Gal4;UAS:nfsb-mCherry)* and *Tg(HuC:GCaMP6s)*, were embedded in 1.5% agarose with their tails freed. We raised and performed all experiments in embryo water maintained at pH 6.5–7.5, which is crucial for ensuring optimal behavioral responses to TRPA1 stimulation. For volumetric two-photon imaging experiments, an electrically tunable lens (Edmund Optics, 83–922) was installed in the light path before the galvanometer scanner to allow fast axial refocusing of the two-photon excitation spot. Images alternating between two or three *z*-planes per fish were acquired at a frame rate of ~237 ms per *z*-plane, corresponding to ~474 ms or ~711 ms per *z* volume, respectively. For TRPA1 photoactivation, fish were stimulated first in DMSO (0.1%) then in optovin (Tocris 4901, 25 μ M in 0.1% DMSO, vortexed and filtered with a 0.45- μ m syringe filter to remove undissolved particles). For both conditions, fish were first incubated in the respective solutions for 5–10 min.

In both DMSO and optovin trials, the tail of the fish was stimulated for 100 ms with a 405-nm laser at 120-s intervals. The laser was focused on the middle of the tail (1 or 7 mW at sample for low or high intensity stimulation), and aligned on non-experimental fish before starting the experiment to prevent unnecessary ultraviolet light exposure in the experimental animals. Long (seconds to minutes) exposure to high intensity ultraviolet laser was observed to abolish or reduce OXT neuron responses to TRPA1 stimulation in some fish, possibly due to ultraviolet-light-induced tissue damage. An electronic shutter (Uniblitz VS25) was installed above the objective to prevent saturation of the photomultiplier tube by the ultraviolet laser. Tail movements were simultaneously monitored under infrared (850 nm) illumination at 200 f.p.s. (Pike F-032 camera, Allied Vision Technology) through a substage optical path, and tail coordinates were extracted online using custom LabVIEW software.

Calcium imaging analysis. All calcium imaging data were analyzed using custom ImageJ and Matlab software. The general protocol for analysis was as follows: (1) Image registration to correct for motion artifacts using the TurboReg plugin⁶³ in ImageJ; (2) extraction of fluorescence signals from both channels using manually segmented ROIs in Matlab; and (3) calculation of $\Delta f/f$ signals from raw traces and alignment to tail traces, as needed, in Matlab.

For fish expressing *Tg(UAS:GCaMP6s)* exclusively in *oxt*-expressing neurons, ROIs were drawn over all visible cells in a maximum projection image for each plane, and raw fluorescence traces were extracted as the mean pixel value within the ROI. For measurements in *Tg(oxt:Gal4;UAS:nfsb-mCherry; elavl3:GCaMP6s)* triple-transgenic animals, ROIs corresponding to OXT neurons were segmented in the red channel and used to extract fluorescence traces from the aligned green channel. The same neurons were selected in DMSO and optovin trials. To measure responses from non-OXT neurons, ROIs were drawn over all visually distinguishable GCaMP neurons in the green channel. $\Delta f/f$ values were calculated from raw traces using the average fluorescence over the time period before the first stimulus as the baseline to which all traces were normalized.

Regressor analysis. To cross-correlate neuron activity with behavior, we generated regressors from six variables: two stimulus variables (DMSO and optovin) and four motor variables corresponding to motor behavior that occurred either within 10 s post-stimulus, or at all other time points, again for both DMSO and optovin. The regressors were convolved with a GCaMP6s kernel based on its measured response delay (0.48 s) and decay time (3 s, based on a previous study⁶⁴) and cross-correlated with calcium traces that had been smoothed with a three-frame zero phase filter. We set a positive threshold of $r = 0.35$ to identify 'active' neurons and a negative threshold of $r = -0.35$ to identify neurons with anti-correlated activities, although we did not observe the latter in our analysis. These thresholds were set based on the distribution of r values obtained from *mCherry*-expressing OXT neurons, which estimate the probability of spurious correlations (that is false positives) caused by motion or other artifacts (Supplementary Fig. 4b).

Optogenetic locomotion experiments. Larvae (6–8 d.p.f.) were embedded in 1.5% agarose with their tails freed, then stimulated using a fluorescence microscope (Olympus BX51WI) equipped with a $\times 40$ water-dipping objective lens. The stimulation area was 150 μ m in diameter (A-stop open, F-stop closed), as visualized by Kaede photoconversion (Fig. 5a). The light intensity at the sample was calibrated to be 6 mW mm⁻². Fish were stimulated for durations of 0.1, 1, 2, 3 and 5 s every 30 s (6 presentations each, randomly shuffled for each fish). OXT mutant clutches were tested using the same protocol and genotyped post-hoc.

For free-swimming optogenetics experiments, 6 d.p.f. larvae were lightly anesthetized in 0.1% MS-222 and the eyes were surgically removed using forceps. Fish were returned to warmed Ringer's solution and allowed to recover for 12 h. Behavioral experiments were performed with the fish placed singly into a 1-inch diameter agarose arena. This arena was placed onto a platform covered with diffusion filter paper, above a blue light-emitting diode (LED) (SP-08-B4, Luxeon) for ChR2 activation and illuminated with an array of 800 nm LEDs. A custom

LabVIEW program was used to control data acquisition and stimulus delivery. Fish location was tracked in Matlab. Ratios of distance traveled during the 5 s pulse divided by the total distance traveled during the pulse plus 5 s baseline period were measured for each fish.

Reduced preparation. Larvae (7 d.p.f.) of the WIK background were embedded in 1.5% agarose in zebrafish ACSF with tails released. A thinned tungsten wire was used to transect the brain above the midbrain–hindbrain boundary. Lack of responses to gentle touch stimuli on the head (at locations anterior to the cut) was used to establish that all forebrain and midbrain tissue had been severed. Transected fish survived for hours in culture solution and produced frequent bouts of small amplitude tail twitches, possibly due to a reduced inhibition of the hindbrain reticulospinal circuitry. We waited at least 5 min after commencement of movement before beginning to record baseline tail movements, then pipetted OXT (Tocris Biosciences, 1910) to a final concentration of 5 μ M 10 min after the start of recording. Uniformly distributed points along the tail of the fish were extracted online at 100 f.p.s. using custom LabVIEW software, and cumulative tail angles were analyzed and plotted analyzed in Matlab.

Calcium imaging of reticulospinal neurons. Zebrafish larvae were backfilled from the spinal cord at 4 d.p.f. with 10% w/v Cal-590 (dextran conjugate 3,000 MW, AAT Bioquest) to label reticulospinal neurons with the red calcium dye. Experiments were performed using 5–7 d.p.f. zebrafish larvae after Cal-590 backfill. Zebrafish larvae were immobilized in 0.1% w/v α -bungarotoxin or 10% formamide and then stabilized on a sylvard-lined glass bottom dish containing extracellular solution (composition in mmol per l: 134 NaCl, 2.9 KCl, 1.2 MgCl₂, 2.1 CaCl₂, 10 HEPES buffer, 10 glucose, adjusted to pH 7.8 with NaOH). The brain was dissected out to remove all sensory inputs from the head with the connection to the spinal cord preserved.

Calcium imaging was performed using an upright microscope (BX51WI, Olympus) with a sCMOS camera (Zyla, Andor DG-152X-C1E-FL) and a mercury arc lamp (X-cite 120, Excelitas). Calcium responses of the reticulospinal neurons were acquired with Solis Software (Andor) at 5–20 f.p.s. and analyzed using ImageJ and Excel.

EMG or motor nerve activity recordings were acquired simultaneously with calcium imaging at 50 kHz with a MultiClamp 700B amplifier, digitized with a DigiData 1550B and analyzed using pClamp 10 software (Molecular Devices) and Dataview (University of St Andrews). The recording electrodes were made with standard wall glass capillaries with a pipette puller (PIP6, HEKA) and the tip was cut to make a 20–50- μ m opening.

For TRPA1 stimulation experiments, wild-type zebrafish larvae were used and optovin was added into the extracellular solution in the recording dish with a final concentration of 25 μ M. A 410-nm violet LED (20–100 ms, 11.7 mW) was used to activate optovin-mediated TRPA1 channel opening. To activate OXT neurons, *Tg(oxt:Gal4;UAS:ChR2-YFP)* zebrafish larvae were used and a 480-nm blue LED (5 s, 2.4 mW mm⁻²) was used to activate the ChR2.

M-cell ablations and behavioral analysis. Fish (5–6 d.p.f.) were anesthetized with MS-222 and backfilled by injection of Texas Red Dextran (ThermoFisher, no. D3329) into the spinal cord. Fish were then allowed to recover overnight in Ringer's solution at 37 °C. The next day, fish were lightly anesthetized with tricaine before being placed onto a two-photon microscope. M-cells were bilaterally ablated using a mode-locked laser (920 nm) as previously described⁵⁵. For sham ablations, the same procedure was followed except that the reticulospinal array was not backfilled and the laser was scanned on an unlabeled section of brain. Tethered behaviors were evaluated before and 1 h after ablation by imaging at 604 Hz using custom LabVIEW software (v.16.0, National Instruments). For optovin trials, a 500-ms pulse of 405-nm light (0.41 mW mm⁻²) was used to stimulate the tail of the fish. For optogenetic experiments, the same spot of 405-nm light was aimed at the head of the fish for 5 s. While the use of a shorter excitation wavelength resulted in shorter response latencies than in other optogenetic experiments, wild-type animals were similarly unresponsive in this protocol. Animals that failed to respond to the stimulus during the baseline period were excluded from the study.

Free-swimming TRPA1 stimulation (mutants and ablations). Fish were singly placed into a 20.6-mm cut-out agarose circular mold illuminated by three quad blue LEDs (Luxeon Star, 470 nm). Following 5 min of habituation in DMSO, fish were stimulated once every 30 s with a 100-ms pulse of blue light. The DMSO solution was then exchanged with optovin, and the same protocol repeated. Behavior was recorded at 200 f.p.s. (Pike F-032, Allied Vision) and analyzed using custom Python software. OXT mutant clutches were genotyped post-hoc. For nitroreductase-mediated ablations, *Tg(oxt:Gal4;UAS:nfsb-mCherry)* fish were incubated in 2.5 mM MTZ (Sigma M-3761) from 4 to 6 d.p.f., then held in facility water until behavioral testing at 8 d.p.f. Ablations were confirmed by confocal imaging (Zeiss LSM800).

Statistics. All bar plots show the mean \pm s.e.m. over fish. The Matlab function notBoxPlot.m (showing mean, 1 standard deviation (s.d.) and 95% confidence intervals) was used to plot data in Figs. 5 and 6 and Supplementary Fig. 9.

Significance was reported as follows: * $P < 0.05$, ** $P < 0.01$ and *** $P < 0.001$. Significance was determined using the nonparametric Wilcoxon signed-rank test for paired data and the Wilcoxon rank-sum test for independent samples. The Wilcoxon signed-rank test was also used in Fig. 1b for comparing the distribution of normalized OXT ROI signals across different behavioral stimuli to the null hypothesis of median 1. In most cases, these tests were two-sided (specified in the figure legends). The nonparametric Kruskal–Wallis test or parametric two-way analysis of variance (ANOVA) was used when comparing fish using multiple parameters or multiple stimulation conditions. Thus, with the exception of two-way ANOVA, for which we made the assumption of normally distributed data, nonparametric tests were used for all analyses. Bootstrapping analysis (Supplementary Fig. 10) was performed with a custom Matlab code by sampling with replacement individual fish, followed by individual bouts per fish, for 10,000 iterations, to generate a distribution of mean differences between pre-sham and post-sham or M-cell ablation behavior. Pearson's correlation was used in regressor and other linear correlation analyses. No statistical methods were used to predetermine sample sizes, but our sample sizes were similar to those reported in previous publications^{19,38,55}. In experiments involving *opt^{-/-}* mutants, the researchers were blinded to the genotype, which was determined post-hoc. No blinding was used in any other experiment, but data were acquired and processed in a highly automated way, often by multiple independent researchers across laboratories.

Reporting Summary. Further information on research design is available in the Nature Research Reporting Summary linked to this article.

Data availability

All data, code (hardware control and analysis) and resources (transgenic lines/mutants generated) will be made available by the corresponding authors upon request.

Code availability

Live versions of the analysis code are maintained at <https://www.github.com/carolinewee>.

References

- Kim, D. H. et al. Pan-neuronal calcium imaging with cellular resolution in freely swimming zebrafish. *Nat. Methods* **14**, 1107–1114 (2017).
- Muto, A. et al. Activation of the hypothalamic feeding centre upon visual prey detection. *Nat. Commun.* **8**, 15029 (2017).
- Davison, J. M. et al. Transactivation from Gal4-VP16 transgenic insertions for tissue-specific cell labeling and ablation in zebrafish. *Dev. Biol.* **304**, 811–824 (2007).
- Miyasaka, N. et al. From the olfactory bulb to higher brain centers: genetic visualization of secondary olfactory pathways in zebrafish. *J. Neurosci.* **29**, 4756–4767 (2009).
- Lacoste, A. M. B. et al. A convergent and essential interneuron pathway for Mauthner-cell-mediated escapes. *Curr. Biol.* **25**, 1526–1534 (2015).
- Scott, E. K. et al. Targeting neural circuitry in zebrafish using GAL4 enhancer trapping. *Nat. Methods* **4**, 323–326 (2007).
- Ben Fredj, N. et al. Synaptic activity and activity-dependent competition regulates axon arbor maturation, growth arrest, and territory in the retinotectal projection. *J. Neurosci.* **30**, 10939–10951 (2010).
- Montague, T. G., Cruz, J. M., Gagnon, J. A., Church, G. M. & Valen, E. CHOPCHOP: a CRISPR/Cas9 and TALEN web tool for genome editing. *Nucleic Acids Res.* **42**, W401–W407 (2014).
- Gagnon, J. A. et al. Efficient mutagenesis by Cas9 protein-mediated oligonucleotide insertion and large-scale assessment of single-guide RNAs. *PLoS One* **9**, e98186 (2014).
- Schindelin, J. et al. Fiji: an open-source platform for biological-image analysis. *Nat. Methods* **9**, 676–682 (2012).
- Altstein, M. & Gainer, H. Differential biosynthesis and posttranslational processing of vasopressin and oxytocin in rat brain during embryonic and postnatal development. *J. Neurosci.* **8**, 3967–3977 (1988).
- Thisse, C. & Thisse, B. High-resolution in situ hybridization to whole-mount zebrafish embryos. *Nat. Protoc.* **3**, 59–69 (2008).
- Thevenaz, P., Ruttimann, U. E. & Unser, M. A pyramid approach to subpixel registration based on intensity. *IEEE Trans. Image Process.* **7**, 27–41 (1998).
- Chen, T.-W. et al. Ultrasensitive fluorescent proteins for imaging neuronal activity. *Nature* **499**, 295–300 (2013).

Reporting Summary

Nature Research wishes to improve the reproducibility of the work that we publish. This form provides structure for consistency and transparency in reporting. For further information on Nature Research policies, see [Authors & Referees](#) and the [Editorial Policy Checklist](#).

Statistics

For all statistical analyses, confirm that the following items are present in the figure legend, table legend, main text, or Methods section.

n/a Confirmed

- The exact sample size (n) for each experimental group/condition, given as a discrete number and unit of measurement
- A statement on whether measurements were taken from distinct samples or whether the same sample was measured repeatedly
- The statistical test(s) used AND whether they are one- or two-sided
Only common tests should be described solely by name; describe more complex techniques in the Methods section.
- A description of all covariates tested
- A description of any assumptions or corrections, such as tests of normality and adjustment for multiple comparisons
- A full description of the statistical parameters including central tendency (e.g. means) or other basic estimates (e.g. regression coefficient) AND variation (e.g. standard deviation) or associated estimates of uncertainty (e.g. confidence intervals)
- For null hypothesis testing, the test statistic (e.g. F , t , r) with confidence intervals, effect sizes, degrees of freedom and P value noted
Give P values as exact values whenever suitable.
- For Bayesian analysis, information on the choice of priors and Markov chain Monte Carlo settings
- For hierarchical and complex designs, identification of the appropriate level for tests and full reporting of outcomes
- Estimates of effect sizes (e.g. Cohen's d , Pearson's r), indicating how they were calculated

Our web collection on [statistics for biologists](#) contains articles on many of the points above.

Software and code

Policy information about [availability of computer code](#)

Data collection

Calcium imaging of OXT neurons and tethered behavioral experiments were performed using custom LabView (2016 version 16.0) Software. Calcium responses of the reticulospinal neurons were acquired with Solis software (4.28.30026.0, SDK: 2.100.33026.0). EMG or motor nerve activity recordings were acquired with using MultiClamp 700B Commander (2.2.0.1) and Clampex (10.7.0.3) Free-swimming behavioral data for Optovin stimulation was collected with custom Python (2.7) software. All other data was acquired using commercial microscopes from Zeiss (LSM800) and Olympus (BX51WI, FVB1000).

Data analysis

Data analysis for calcium imaging and M-cell ablations was performed using custom MATLAB (R2017a and R2018b) software. pERK analysis was performed using custom FIJI/Image J (2.00-rc-43) and MATLAB (R2017a) software. Free-swimming behavioral experiments were analyzed using custom Python (2.7) software. Calcium imaging data of reticulospinal neurons were analyzed with ImageJ (1.52i) and Excel (2016) software. EMG recordings were analyzed using pClamp 10 software (Clampfit 10.7.0.3) and Dataview (University of St Andrews, 11.0.0).

For manuscripts utilizing custom algorithms or software that are central to the research but not yet described in published literature, software must be made available to editors/reviewers. We strongly encourage code deposition in a community repository (e.g. GitHub). See the Nature Research [guidelines for submitting code & software](#) for further information.

Data

Policy information about [availability of data](#)

All manuscripts must include a [data availability statement](#). This statement should provide the following information, where applicable:

- Accession codes, unique identifiers, or web links for publicly available datasets
- A list of figures that have associated raw data
- A description of any restrictions on data availability

All data can be made available by authors.

Field-specific reporting

Please select the one below that is the best fit for your research. If you are not sure, read the appropriate sections before making your selection.

Life sciences Behavioural & social sciences Ecological, evolutionary & environmental sciences

For a reference copy of the document with all sections, see [nature.com/documents/nr-reporting-summary-flat.pdf](https://www.nature.com/documents/nr-reporting-summary-flat.pdf)

Life sciences study design

All studies must disclose on these points even when the disclosure is negative.

Sample size	No statistical methods were used to predetermine sample sizes but our sample sizes are similar to those reported in previous publications.
Data exclusions	For M-cell ablation experiments, 3 fish that were minimally responsive during the baseline period in Optovin were excluded from analysis. Fish that were unresponsive after M-cell ablations were excluded from kinematic analysis. No other data were excluded from the analysis.
Replication	Before collecting the final dataset for this revision, other sets of data were acquired, including on different microscopes and with different experimenters and in two different laboratories (Engert and Douglass), and results were highly reproducible across all these conditions.
Randomization	In experiments that required randomization (e.g. pERK), larvae were randomly assigned to each condition. For other experiments, within sample controls were used.
Blinding	Investigators were only blinded for oxytocin mutant experiments, since post-hoc genotyping was performed. Otherwise data collection and analysis was not blinded, but often acquired by multiple researchers and processed in a highly- automated fashion.

Reporting for specific materials, systems and methods

We require information from authors about some types of materials, experimental systems and methods used in many studies. Here, indicate whether each material, system or method listed is relevant to your study. If you are not sure if a list item applies to your research, read the appropriate section before selecting a response.

Materials & experimental systems

n/a	Involved in the study
<input type="checkbox"/>	<input checked="" type="checkbox"/> Antibodies
<input checked="" type="checkbox"/>	<input type="checkbox"/> Eukaryotic cell lines
<input checked="" type="checkbox"/>	<input type="checkbox"/> Palaeontology
<input type="checkbox"/>	<input checked="" type="checkbox"/> Animals and other organisms
<input checked="" type="checkbox"/>	<input type="checkbox"/> Human research participants
<input checked="" type="checkbox"/>	<input type="checkbox"/> Clinical data

Methods

n/a	Involved in the study
<input checked="" type="checkbox"/>	<input type="checkbox"/> ChIP-seq
<input checked="" type="checkbox"/>	<input type="checkbox"/> Flow cytometry
<input checked="" type="checkbox"/>	<input type="checkbox"/> MRI-based neuroimaging

Antibodies

Antibodies used	The rabbit anti-oxytocin antibody (VA10, 1:5000) from Harold Gainer's lab was a gift from Lauren O'Connell. All other materials are available from standard commercial sources stated in the methods section. They are 1) Rabbit anti-oxytocin (AHP371, AbD Serotec (now BioRad), 1:300), 2) Rabbit anti-pERK and mouse anti-ERK (tERK) antibodies (Cell Signaling, #4370 and #4696, 1:500) 3) Alexafluor secondary antibodies (1:500).
Validation	The rabbit anti-oxytocin antibody from Harold Gainer's lab was validated in Altstein and Gainer (1988). The commercial rabbit anti-oxytocin (AHP71) was validated in the following references: 1. Suzuki, S. & Handa, R.J. (2005) Estrogen receptor-beta, but not estrogen receptor-alpha, is expressed in prolactin neurons of the female rat paraventricular and supraoptic nuclei: comparison with other neuropeptides. <i>J Comp Neurol.</i> 484: 28-42. 2. Welch, M.G. et al. (2009) Expression and developmental regulation of oxytocin (OT) and oxytocin receptors (OTR) in the enteric nervous system (ENS) and intestinal epithelium. <i>J Comp Neurol.</i> 512: 256-70. The anti-pERK and ERK antibodies were validated in Randlett et al, 2015.

Animals and other organisms

Policy information about [studies involving animals](#); [ARRIVE guidelines](#) recommended for reporting animal research

Laboratory animals	5-8 dpf AB, Nacre (mitfa ^{-/-}) fish (in AB background) or WIK laboratory strains of zebrafish were used. Other transgenic lines used were generated on the AB background and are specified in the methods section.
Wild animals	The study did not involve wild animals.

Field-collected samples

The study did not involve field-collected samples.

Ethics oversight

IACUC at Harvard and University of Utah

Note that full information on the approval of the study protocol must also be provided in the manuscript.